PHASE STRUCTURED WAVEFIELDS WITH PHASE SINGULARITIES AND BISPECTRAL PROPERTIES

by

Marco Scipioni

A dissertation submitted to the faculty of
The University of North Carolina at Charlotte
in partial fulfillment of the requirements
for the degree of Doctor of Philosophy in
Optical Science and Engineering

Charlotte

2010

Approved by:

Dr. Robert K. Tyson

Dr. Michael A. Fiddy

Dr. Greg Gbur

Dr. Jacek Dmochowski

ABSTRACT

The work presented in this dissertation can be subdivided into two parts. The first part illustrates the novel use of a 37 actuator segmented deformable mirror for the creation of optical vortex beams ranging in topological charge from 1 to 10. The segmented deformable mirror offers a dynamic, polarization independent alternative for creating vortex beams with arbitrary charge. An optical vortex mode purity comparison between the deformable mirror and multi-step diffractive phase plates with 16 and 32 discrete steps is carried out both analytically and in simulation. Computer simulations show the intensity and phase of the vortices generated with the two methods. The deformable mirror, by being reconfigurable, shows better mode purity for high charge OVs, while the static phase plate mode efficiency declines due to the fixed number phase quantization.

The second part of the dissertation reviews the concept of the bispectrum (3^{rd} order polyspectrum) and the possibility of creating partially spatially coherent beams with nonzero bispectral characteristics. Numerical simulations show that bispectral properties encoded in an input wavefield are invariant upon propagation in free space.

This result opens the possibility of using the bispectrum as a new degree of freedom for encoding information in a wavefield.

ACKNOWLEDGMENTS

I thank my advisor Dr. Robert K. Tyson for his guidance and for allowing me all the scientific freedom I asked to explore and learn about a variety of topics during the course of my research.

I am grateful to my committee members, Dr. Michael A. Fiddy and Dr. Greg Gbur, for always making time for my questions every time I knocked at their office door and for offering thoughtful criticism on my dissertation work.

Infinite gratitude goes to my parents for valuing education and giving me the privilege to pursue my doctoral degree.

I would also like to thank my friends at the university and outside the University for all the listening and brainstorming we had together. Thanks to my fiancée Aundrea for steadily supporting me through my dissertation journey and for her constant encouragement.

TABLE OF CONTENTS

LIST OF FIGURES

CHAPTER 1: INTRODUCTION

1.1 INTRODUCTION

Electromagnetic wavefield properties can be manipulated in order to tailor the field's profile to specialized applications. This dissertation focuses on wavefields that exhibit nontrivial phase structures. It has been demonstrated that the phase construction significantly influences the field behavior.

Optical vortex beams are electromagnetic wavefields with peculiar phase structure: they contain phase singularities and have helicoidal wavefronts. They present high robustness and self-healing properties upon propagation in disturbing media.

There are a growing number of applications that take advantage of the beneficial properties of optical vortex beams. That leads to the development of new and enhanced methods for the generation of wavefields containing optical vortices.

This dissertation presents the novel and successful use of a 37 actuator segmented deformable mirror for the generation of optical vortex beams with topological charge from 1 to 10. The segmented deformable mirror is shown to be a viable alternative to other existing methods for creating vortex beams. The incessant progress in segmented deformable mirror technology is an assurance of improved performance for deformable mirrors in terms of vortex beam generation capability. New dielectric coatings will extend the use of segmented DMs and optical vortex fields to high power application

where other methods are less suitable. There is work in progress that aims at changing the segments' shape at the phase jump discontinuity from hexagonal to rectangular in order to generate better vortices.

The deformable mirror offers several advantages over other methods: it is a dynamic, polarization and wavelength independent device.

An optical vortex mode purity comparison between the mirror and multi-step diffractive phase plates (SPP) with 16 and 32 discrete steps was carried out both analytically and in simulation in order to quantify the DM performance.
The comparison represents the metric used to support the adoption of the DM for vortex beam applications.

Computer simulations show both the intensity and phase profile of the vortex fields generated by the DM and SPP. The dynamic deformable mirror can generate optical vortices with higher mode purity, while the static phase plate mode efficiency declines due to the phase steps quantization. The mode purity comparison serves to evaluate the performance of the DM for applications based on high topological charge optical vortex fields. My results conclude that the DM is a versatile device that can be used in applications that employ vortex fields.

The final part and contribution of this research was to introduce the possibility of creating phase structured wavefields with nonzero bispectral characteristics. These wavefields show an intrinsic statistical phase structure due to the presence of quadratic phase coupling in the field angular momentum and consequential nonzero bispectrum.

The concept of bispectrum (3^{rd} order polyspectrum) is used to create a probabilistic wavefield model. So far the bispectrum has been mostly used as a statistical tool to characterize the nonlinear properties of systems and signals.

I encoded a specific bispectral signature in the input partially spatially coherent wavefield. The field was then propagated in free space. Numerical simulations showed that the bispectral signature remains perfectly intact and invariant upon propagation. This result can be exploited to design partially spatial coherent wavefields with nonzero bispectrum and create new fields with improved propagation characteristics. The bispectral wavefields do not need to be just a theoretical proposition: a 4-F spatial filtering system can be efficiently used to experimentally generate partially coherent fields with nonzero bispectrum.

My analysis and result support the conclusion that the bispectrum and its spatial counterpart, the 3-point autocorrelation, behave as "coherence waves" and travel undisturbed through free space as realized by other authors in the past. I reintroduced the bispectrum as a new degree of freedom for encoding information in a wavefield and verified this concept using a bispectral design where quadratic phase coupling was applied to spectral components arranged in a symmetric circular configuration.

1.2 OPTICAL VORTICES

Singular Optics is a rapidly developing branch of optics that investigates anomalous features like phase and polarization singularities in wavefields. These mathematical anomalies where certain field properties fail to be defined are actually not that anomalous: it turns out that singular field behaviors are very common and

mathematically generic in real life interference phenomena like speckle fields. Optical vortices probably represent the most popular and studied singular optics topic.

An optical vortex (also known as a screw dislocation or phase singularity) is a zero of an optical field, a point of zero intensity [1]. Light is twisted like a corkscrew around its axis of propagation [2,3]. Because of the twisting, the light waves at the axis itself cancel each other out. An optical vortex looks like a ring of light, with a dark hole in the center. The vortex is given a number, called the topological charge ℓ, related to the orbital angular momentum of the field. The wavefront of an optical vortex is a continuous surface consisting of ℓ embedded helicoids, each with $\ell\lambda$ pitch, spaced from each other one wavelength λ. As an example, Figure 1.1 represents the wavefront of a charge $\ell = 3$ vortex propagating along the z-axis, illustrating the three intertwined helicoids.

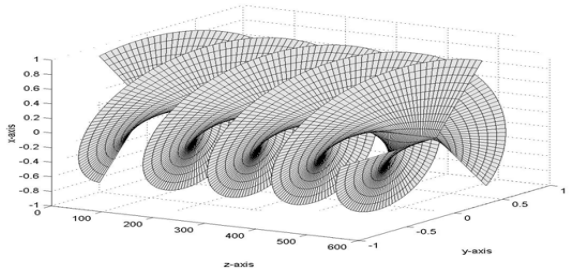

Fig.1.1 Wavefront of an optical vortex with charge 3=ℓ (arbitrary spatial units)

Fig. 1.2 Transverse vortex phase profile.

The generalized functional form for a field hosting an optical vortex is, in a plane transverse to propagation direction, locally given by

$$f(r,\theta) = A(r,\theta)e^{i\ell\theta} \tag{1.1}$$

where $A(r,\theta)$ can be any square integrable, continuous and smooth complex amplitude wave function in cylindrical polar coordinates. The phase argument θ represents the distinctive, transverse vortex phase profile, impressing a linear phase increase in the azimuthal direction to the field. The charge of a vortex can be an integer or fraction, and also positive or negative, depending on the handedness of the twist. Figure 1.2 shows a map of the phase profile of a vortex beam. The phase jumps by a value $\ell 2\pi$ at the discontinuity.

Vortex beams have been successfully employed in optical tweezers applications [8,11], because they offer the advantage of trapping and spinning low index (with respect to the hosting medium) dielectric particles in their zero intensity region. Vortex carrying beams also have interesting potential for use in free-space optical communications [4,5,7]. Of particular interest is the ability of vortex beams to conserve their charge through atmospheric turbulence [12]. Also, vortex beams "self-heal" around obstacles [13], and experiments have shown that vortices are conserved through fog [14]. These properties make it an ideal extension to conventional coding schemes such as on-off keying or coherent modulation techniques.

1.3 ZEROS OF VECTOR WAVEFIELDS

The study of wavefields containing optical vortices is usually based on the scalar theory assumption. In the paraxial approximation there are solutions to the paraxial vector wave equation in which the direction of the electric field E is spatially non-

homogeneous: the electric field polarization is a function of transverse position r in the beam. These solutions present points of zero intensity the same way as field with optical vortices do. No matter the type of wavefield, a zero of intensity is always a phase singularity. However these vector beams do not necessarily have optical vortices: the phase landscape surrounding the zeros does not need to have an azimuthal variation.

Beams with azimuthal or radial polarization are examples of beams with intensity zeros that are not optical vortices. The zeros of intensity arise because the electric field oscillates simultaneously in all directions and destructive interference occurs. The phase in this case is not undefined: it is the linear polarization that is undefined.

This does not mean that paraxial wavefields with radial or azimuthal polarization cannot contain optical vortices. But if the wavefield is linearly polarized a zero of intensity can only occur if an optical vortex is present.

1.4 ANGULAR MOMENTUM OF RADIATION

It is well established that electromagnetic radiation carries both energy and momentum which can be exchanged with matter upon interaction. Electromagnetic phenomena are generally modeled using two complex-valued vector fields, the electric field $\mathbf{E}(\mathbf{r},t)$ and the magnetic field $\mathbf{B}(\mathbf{r},t)$. These two fields are interrelated via four partial differential equations, Maxwell equations, from which two wave equations, one for $\mathbf{E}$ and one for $\mathbf{B}$, can be derived. That is an the mathematical evidence that electromagnetic radiation is a wave-like phenomenon and that $\mathbf{E}$ and $\mathbf{B}$ are capable of transporting energy. Classical electromagnetic theory treats electromagnetic radiation as a continuum which is best described in terms of density functions. The electromagnetic

energy density (energy per unit volume) $w(\mathbf{r},t)$, defined in terms of the complex $\mathbf{E}(\mathbf{r},t)$ and $\mathbf{B}(\mathbf{r},t)$, is

$$w(\mathbf{r},t) = \frac{1}{2}[\varepsilon_0 |\mathbf{E}(\mathbf{r},t)|^2 + \frac{1}{\mu_0}|\mathbf{B}(\mathbf{r},t)|^2] \tag{1.2}$$

In vacuum, $|\mathbf{B}(\mathbf{r},t)| = |\mathbf{E}(\mathbf{r},t)|/c$ where $c = \frac{1}{\sqrt{\varepsilon_0\mu_0}}$ is the speed of light. The electromagnetic energy is equiparted between the electric and magnetic fields. The fields $\mathbf{E}(\mathbf{r},t)$ and $\mathbf{B}(\mathbf{r},t)$ also serve to compose a very useful vector quantity representing the energy-current density (energy flux) of electromagnetic radiation:

$$\mathbf{S}(\mathbf{r},t) = \frac{1}{\mu_0}[\mathbf{E}(\mathbf{r},t)\times\mathbf{B}(\mathbf{r},t)] \tag{1.3}$$

The vector $\mathbf{S}(\mathbf{r},t)$ is called the Poynting vector and has units (W/m^2). This vector is directly related to the concept of radiation pressure ($P_{rad} = \frac{<\mathbf{S}>}{c}$), and its magnitude quantifies energy flux per unit area per unit time. The wavefield linear momentum density $\mathbf{g}$ (linear momentum per unit volume) of the electromagnetic field is given by

$$\mathbf{g} = \varepsilon_0 <[E(\mathbf{r},t)\times B(\mathbf{r},t)]> = \frac{<\mathbf{S}(\mathbf{r},t)>}{c^2} \tag{1.4}$$

where <> represent the time averaging operation. The total linear momentum of an electromagnetic field is given by an integral over the volume occupied by the field:

$$\mathbf{G} = \int \mathbf{g} dV$$

(1.5)where dV is the elementary volume. After defining electromagnetic linear momentum it comes natural to discuss the angular momentum density of an electromagnetic field given by

$$\mathbf{l} = \mathbf{r} \times \mathbf{g} \tag{1.6}$$

where $\mathbf{r}$ is the arm vector from the arbitrarily chosen coordinate system origin and $\mathbf{g}$ is the field linear momentum density. The total angular momentum contained in a wavefield is

$$\mathbf{L} = \varepsilon_0 \int (\mathbf{r} \times \mathbf{g}) dV \tag{1.7}$$

In the case of monochromatic fields with time dependence $e^{-i\omega t}$ (ω is the angular frequency), after several vector manipulations and using Maxwell's equation $\mathbf{B} = \frac{1}{i\omega} \nabla \times \mathbf{E}$, the time-averaged vector $\mathbf{L}$ turns out to be

$$< \mathbf{L} >= \varepsilon_0 \int <(\mathbf{r} \times \mathbf{g}) > dV =$$

$$= \frac{\varepsilon_0}{4\omega i} \int \{\mathbf{r} \times [(\mathbf{E}^* (\nabla \times \mathbf{E}) + \mathbf{E} \times (\nabla \times \mathbf{E}^*)]\} dV \tag{1.8}$$

Our interest in paraxial wavefields propagating along the $z-$direction leads us to focus on the $z-$components of $\mathbf{L}$ for paraxial fields, which is derived to be equal to

$$< \mathbf{L_z} >= \frac{\varepsilon_0}{2\omega i} \int [E_j^* (\mathbf{x} \times \nabla)_z E_j + (\mathbf{E}^* \times \mathbf{E})_z] dV \tag{1.9}$$

It is helpful to express the first addend in the integrand of $< \mathbf{L_z} >$ in polar coordinates (r,ϕ) and the second addend in Cartesian coordinates (x,y) in order to gain insight in the angular momentum generation mechanisms. The quantity $< \mathbf{L_z} >$ then becomes

$$< \mathbf{L_z} >= \frac{\varepsilon_0}{2\omega i} \int [E_j^* \frac{\partial E_j}{\partial \phi} + E_x^* E_y - E_y^* E_x] dV \tag{1.10}$$

The term $\frac{\partial E_j}{\partial \phi}$ suggests that angular momentum will exist in a paraxial field if any of the $\mathbf{E}$ field components vary with the position coordinate ϕ. This first type of angular

momentum contribution is called "orbital"' angular momentum and depends solely on the phase structure of the wavefield, regardless of the polarization state. The second portion of the integrand $,(E_x^* E_y - E_y^* E_x)$, corresponds essentially to the fourth Stokes parameter which measures the degree of elliptical polarization and depends on relative phase and amplitude of field components. This angular momentum contribution is called the "spin " angular momentum of the wavefield. Beth in the 1930s conducted an experiment using a quarter wave plate and showed that circularly polarized light has angular momentum of $\hbar\sigma$ per photon, where $0<|\sigma|<1$ for elliptical polarization, $|\sigma|=0$ for linear polarization and $|\sigma|=1$ for circular polarization. In order to fully appreciate the nature of orbital angular mometum it is important to draw attention to the fact that a general paraxial wavefield is never a pure transverse wavefield (TEM) like wavefields existing in waveguides. Any paraxial field must have a longitudinal field component E_z along the propagation direction z besides its transverse components E_x, E_y. The longitudinal component is in general significantly smaller in magnitude than the transverse components. The existence of the longitudinal field component E_z is indispensible for the existence of orbital angular momentum in the $z-$direction: the azimuthal component of the Poynting vector $\mathbf{S}$, S_ϕ, circulates around the propagation axis z and gives rise to orbital angular momentum. The orbital angular mometum density is given by

$$l_z = \frac{1}{c^2}(\mathbf{r}\times<\mathbf{S}>)_z = \frac{r}{c^2}<S_\phi>=\frac{r}{c^2}<(\mathbf{E}\times\mathbf{B})_\phi> \qquad (1.10)$$

and $<\mathbf{E}\times\mathbf{B}>_\phi \neq 0$ only if $E_z(x,y,z)\neq 0$ (or $B_{radial}(x,y,z)\neq 0$). Optical vortex beam is an umbrella term that encompasses all those paraxial wavefields (Laguerre-Gauss,

Bessel-Gauss, Mathieu-Gauss,etc...) with a transverse, azimuthal phase profile and phase singularity at their center. Optical vortices carry orbital angular momentum due to their azimuthal phase variation.

Optical wavefields oscillate at temporal frequencies that are too large for the current measuring devices to keep up with the instataneous field amplitude or irradiance.

A direct observation of the instantaneous irradiance can instead be performed in the radio or microwave regime. In that regime the instantaneous irradiance of a vortex field with charge $|\ell|=1$ and charge $|\ell|=2$ is given by two and four rotating lobes respectively as illustrated in the figure 1.4 below:

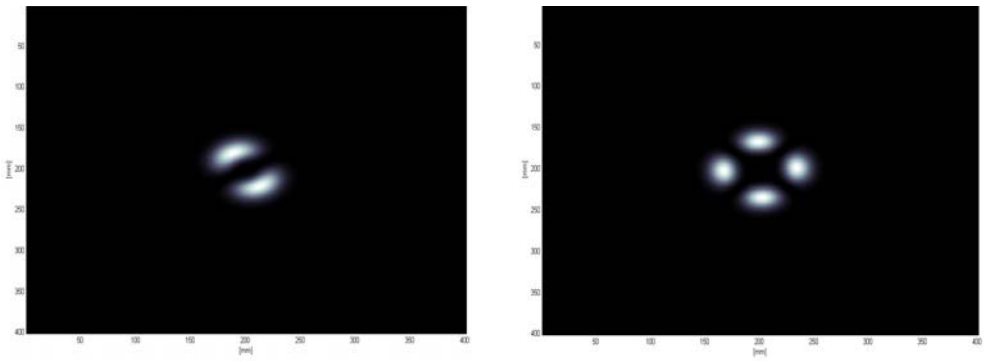

Fig. 1.3 Instantaneous irradiance for a vortex Field with $|\ell|=1$ (left), and $|\ell|=2$ (right).

At optical frequencies the lobed patterns rotate so fast that it is only possible to record the time averaged intensity. The vortex irradiance patterns result in closed rings:

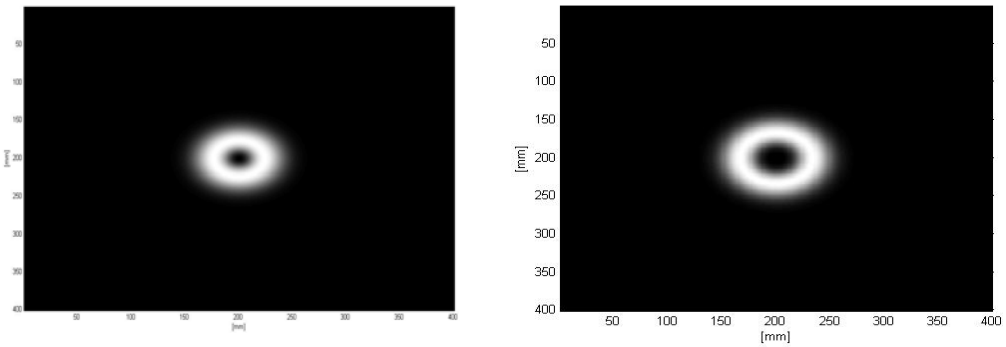

Fig. 1.4.Time-averaged irradiance patterns for $|\ell| = 1$ (left), and $|\ell| = 2$ (right) vortex fields.

Another important aspect worth remembering is that the presence of orbital angular momentum cannot be always associated with the presence of phase singularities: there are wavefields with nonzero orbital angular momentum that do not have phase singularities. Astigmatic Gaussian beams and twisted beams in general are an example. These fields have elliptical irradiance cross section instead of circular cross section. The constant intensity ellipses and iso-phase ellipses are oriented at an angle with respect to each other. The orientation between the ellipses changes over free space propagation causing energy rotation within the field [23,24].

From the photon perspective, orbital angular momentum is always quantized to integer multiples ℓ of $\hbar$, where ℓ is the signed integer indicating the strength of the phase singularity and equal to the number of 2π phase increments gained by the phase around the beam axis. In optical vortex beams the azimuthal momentum per photon is always equal to $\frac{\ell\hbar}{r}$ where r is the radial distance from the beam center. Beams that are not optical vortices but carry orbital angular momentum do not necessarily respect this relation.

CHAPTER 2: EXPERIMENTAL GENERATION OF OPTICAL VORTICES

2.1 METHODS OF GENERATION OF OPTICAL VORTICES

Optical vortices can be generated in a number of ways. We briefly review the methods here. Details of the methods and operation are found in the citations.

A. *Spatial Light Modulators*

One commonly used device for their generation of an optical vortex is the liquid crystal spatial light modulator (LC SLM) [8]. Commercial LC SLMs are either optically or electrically addressed and can modulate the amplitude, the phase, or both for an incident input field. Their main strength is that they are dynamically reprogrammable.

Nematic SLM, the most common, have a time response of roughly 60Hz. When an SLM is used, any significant incident beam power must be distributed, in order to avoid boiling the liquid crystal element, so the amount of incident power can be a limitation.

In the case of amplitude-only spatial light modulators, an optical vortex of a given charge and wavelength can be made from a computer generated hologram (CGH) [8]. Computer-generated holograms are the digitally calculated interferograms between a plane wave beam and a beam carrying an optical vortex. The resulting CGH resembles a diffraction grating with a characteristic "fork" dislocation having the number of prongs in the fork directly related to the topological charge of the design vortex

(number of prongs = desired topological charge+1). The interference is called a fork pattern because the central constructive interference fringe splits into constructive interference prongs pictorially looking like the multi-prong utensil. The CGH is then is applied to the spatial light modulator.

In the case of phase-only spatial light modulators, the phase profile is the sum of the desired optical vortex phase and a phase tilt needed to steer the reflected incident beam away from the direction of incidence. The result is a blazed phase grating that still has a fork feature in its center. Because the blazed phase grating is not perfect, multiple diffraction orders appear after the beam is reflected off the SLM. The first diffraction order contains the optical vortex with the desired topological charge and is the most intense diffraction order. The zero diffraction order is the specular reflection off the SLM. The other diffraction orders are vortex beams with topological charge equal to the diffraction order number multiplied by the topological charge of the desired vortex beam.

B. Mode Converters

Hermite-Gaussian laser modes form an orthogonal family of laser beams. An appropriately weighted superposition of two Hermite-Gauss beams, with the right mode order, can result in a Laguerre-Gauss beam carrying an optical vortex of the desired topological charge at its center. The superposition is achieved through a system of cylindrical lenses by making use of the Gouy effect [12]. This set-up presents alignment challenges and requires high order Hermite-Gauss beams to obtain high order vortex beams, thus limiting the flexibility of the configuration.

C. Helical Mirror

A helical mirror was recently proposed [14] to create optical phase singularities of various topological charges. The mirror shape, controlled by a piezoelectric actuator, provides a continuous phase variation along the azimuthal direction, but also introduces radial phase variations, because of unavoidable material stresses, thus lowering the quality of the generated vortex beams.

D. Dielectric Wedges

By stacking dielectric wedges [13], it was shown to be possible to create a system capable of producing optical vortices of topological charge higher than one. The charge of the vortex beams corresponds to the number of wedges used in the system.

E. Spiral phase plates

A simple, adjustable spiral phase plate has also been used to create vortex beams [10]. The plate is constructed from a parallel-sided transparent plate with polished surfaces in which a crack is induced starting at one edge and terminating close to its center.
Static spiral phase plates (SPPs) are very common. They are spiral-shaped pieces of crystal or plastic that approximate the ideal spiral with a discrete number of phase steps. SPPs are engineered specifically to the desired topological charge and incident wavelength [11,12]. They are efficient, yet expensive, and show high topological charge purity only for low topological charge ℓ [11,14].

F. Deformable mirrors

A deformable mirror (DM) can be used to generate a vortex. A conventional continuous faceplate DM is not well-suited for this action because the surface must have a discontinuous line (not necessarily straight) between the singularity and the edge. On the

other hand, a segmented DM, with discontinuities already in place between the segments, can be formed into a vortex shape, which is transferred to the phase of a beam reflecting from the surface.

If, at the discontinuity, the surface jumps one-half of the wavelength of the light, the reflected beam will have a phase jump of one full wave, and the beam will have a vortex charge $\ell = 1$. By simply multiplying the amplitudes of the segment pistons and tilts, we can apply any charge to the beam up to the mechanical limits of the DM. This allows us a great variability of charge and even fractional charges. Because the mirror is simply a reflecting surface, it can be used at multiple wavelengths.

2.2 RESULTS WITH A SEGMENTED DEFORMABLE MIRROR

We have performed a number of experiments with our 37-segment deformable mirror and have shown that we can generate a vortex. We can vary the charge and have verified the charge in the pupil plane and in the far-field after propagation. The device used to demonstrate vortex generation is the Iris AO S37-X segmented deformable mirror [16]. See Figure 2.1. The S37-X deformable mirror is fabricated with micromachining technology, making it a compact, low mass modulator. The 3.5 mm aperture DM consists of 37 hexagonal segments tiled into an array.

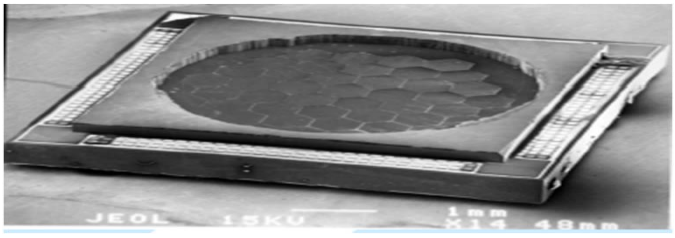

Fig.2.1 Iris AO S37-X segmented deformable mirror.

The DM segment consists of an actuator platform elevated above the substrate as a result of engineered residual stresses in the bimorph flexures. The actuator platform and underlying electrodes form parallel plate capacitors. Placing a voltage across the capacitors generates Coulombic forces that pull the segment towards the substrate. By varying the voltages on the lower electrodes, the actuator can move in piston (pure vertical), tip and tilt directions. The forces are solely attractive, so bidirectional actuation is achieved by biasing the segment at the half-way point.

The maximum stroke is around 5 μm with ±5 mrad tip/tilt. The DM also shows good temperature resistance with peak to valley bow of 0.56 nm/C.

Electrostatic actuation has a nonlinear response between position and voltage. Furthermore, the segment piston/tip/tilt positions are coupled, making the position versus voltage response more complicated. Iris AO has developed a controller that linearizes this response. The user simply enters desired piston/tip/tilt positions and the controller, using a calibrated model, determines the required voltages and sets them on the drive electronics. The controller has demonstrated open-loop positioning of 30 nm rms residual surface figure errors. Thus, a vortex can be created with the DM in open-loop operation.

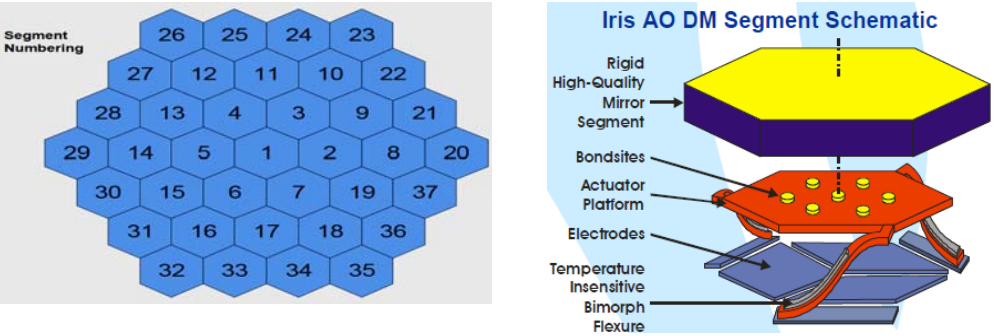

Fig. 2.2 DM Segment numbering (left) and segment anatomy (right)

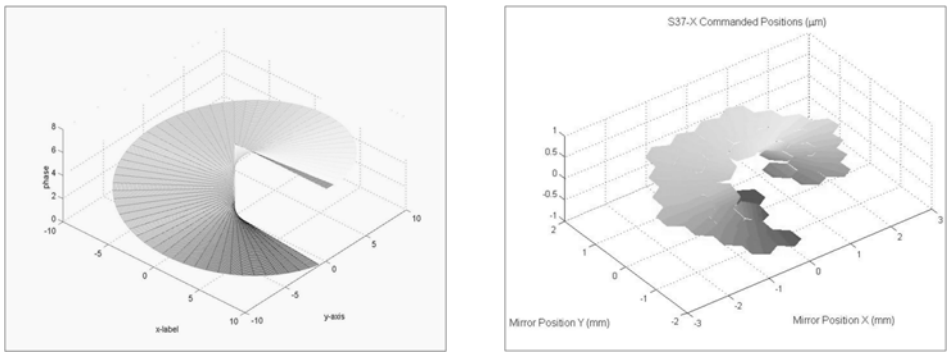

Fig. 2.3 (a) Ideal linear spiral ramp and (b) ramp approximated by Iris AO deformable mirror.

Figure 2.3(b) shows the spiral ramp generated by the DM compared to the ideal, smooth spiral vortex ramp.

Beams carrying topological charge $|\ell| > 1$ are highly unstable to small symmetry-breaking azimuthal perturbations and decompose, upon propagation, into elementary charge vortices of the same sign, symmetrically distributed around the center of the beam, thus conserving the initial net topological charge [2,3]. Astigmatism in the beam or small defects in the diffracting/reflecting optical device are the probable causes of this fragmentation.

Figure 2.4 illustrates the unfolding. A dipole in Figure 2.4 (b), a tripole in Figure 2.4(c), and quadrupole in Figure 2.4(d) are shown from the decay of charge 2, 3, and 4 optical vortex beams created with the Iris AO deformable mirror.

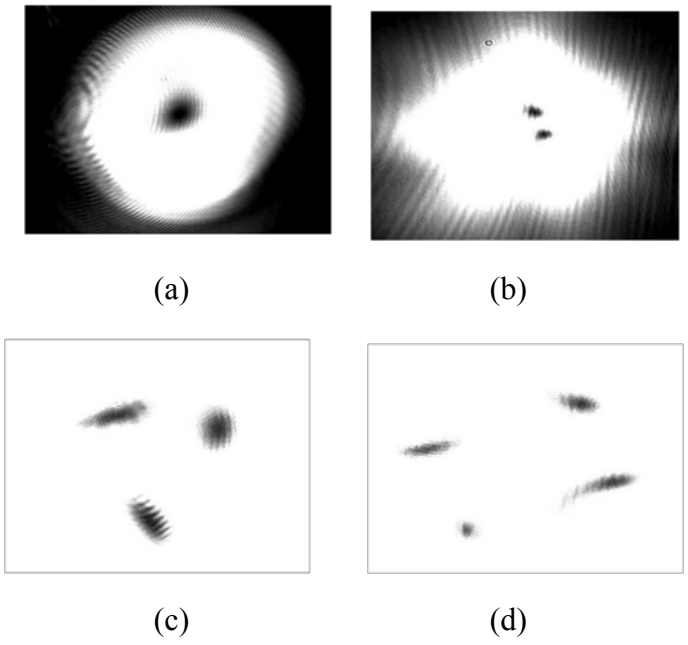

Fig. 2.4 Decay of multiple –charge optical vortices into charge 1 vortices: (a) charge=1; (b) charge=2; (c) charge= 3 (close-up view); (d) charge=4 (close-up view);

We also verified the optical charge from interference patterns in the pupil plane. The interference patterns between a reference plane wave and a beam carrying optical vortices were generated by using a Michelson interferometer.

The resulting interference patterns shown in Figure 2.5 reveal the typical fork pattern which is an indicator of the presence of the phase singularities in the beam reflecting off the deformable mirror.

In Figure 2.5(b) the interference fringes represent the deformable mirror commanded to a flat profile. In Figure 2.5(d) the two-pronged fork pattern for a charge 1 vortex is shown and in agreement with the simulation. For Figure 2.5(f), we placed amplitudes on the deformable mirror that would generate a charge 5 optical vortex. The simulated and

experimental patterns are different because, upon the short propagation length within the interferometer (a few centimeters), the charge 5 vortex apparently unfolded into 5 elementary charge 1 vortices, as expected. We interpret the interference pattern to be the presence of 5 two-pronged forks within the pattern, indicating the presence of a charge 5 vortex.

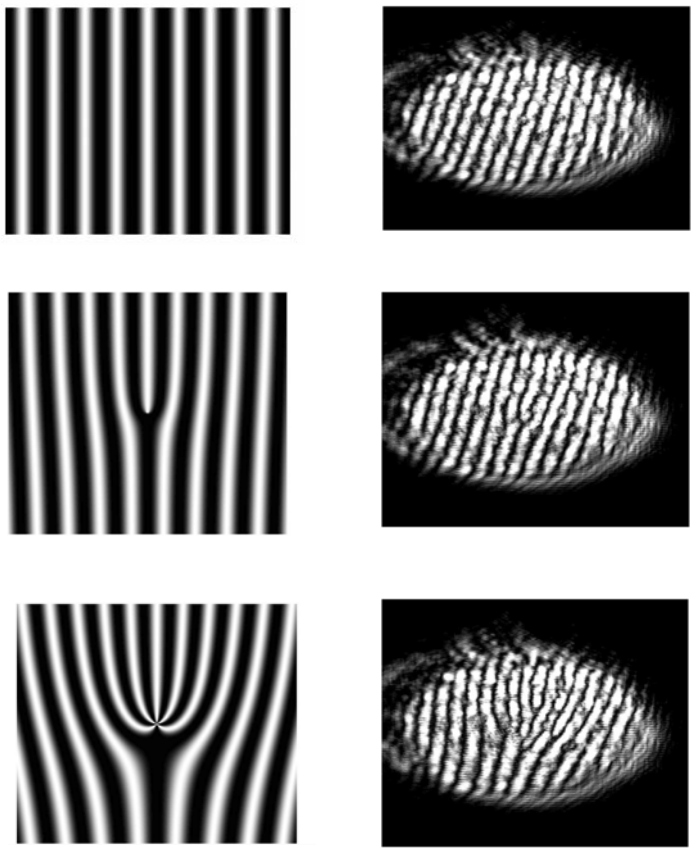

Fig. 2.5 Interference pattern (simulated (left) and experimental (right)) between reference plane wave and plane wave reflected off deformable mirror illustrating fork patterns due to the phase singularities present in the beam.

Optical vortices with half-integer topological charge exhibit, in the near field, a radial line of low intensity attributed to the presence of a chain of charge 1 vortices of alternating sign along the radial phase discontinuity [20,21].

In the far field, however, only a finite number of same-sign vortices appear near the beam axis [18,19]. The number results from rounding the fractional charge ℓ of the vortex to the nearest higher integer. For example, if $\ell = 0.5$, the far field will show one charge 1 vortex, and similarly, three charge 1 vortices if $2.5 \le \ell < 3.5$. The intensity pattern of a beam with fractional topological charge resembles a broken ring.

In Figure 2.6, each dark region indicates the presence of an optical vortex in the field. By increasing the height of the phase discontinuity in discrete increments, it is interesting to follow the evolution of the intensity of the beam as the discontinuity changes from one integer value of the wavelength to the next higher one. It is apparent from Figure 2.6, as predicted from theory [20,21], that as the discontinuity passes a half integer value of the wavelength λ, a new vortex fully appears in the beam, migrating from the periphery along the radial phase discontinuity, to the central area of the beam.

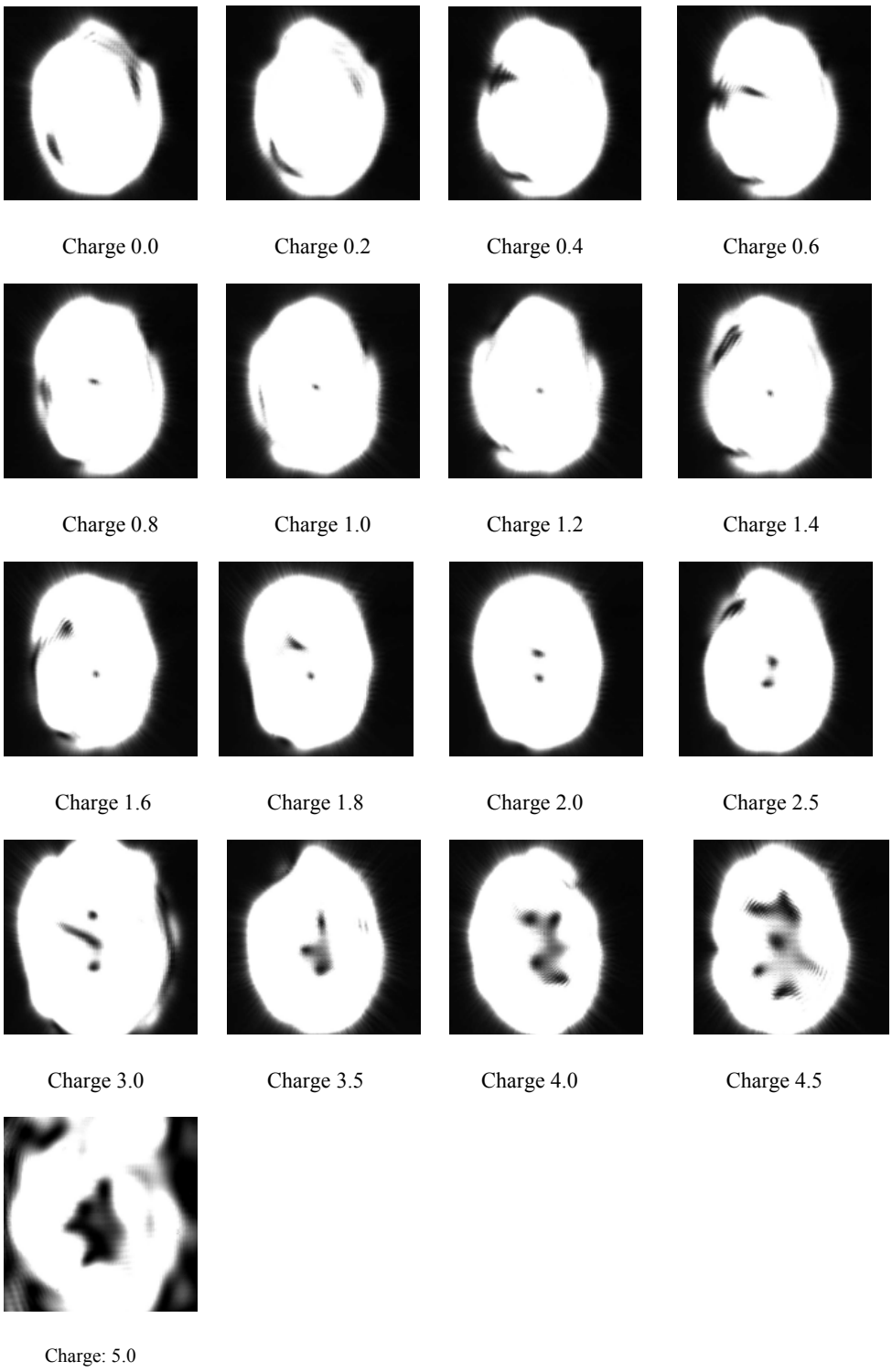

Fig.2.6. Evolution of the intensity pattern for the beam reflected off the deformable mirror from charge 0.0 to charge 5.0 obtained by gradually increasing the phase discontinuity.

2.3 CONCLUSIONS

We made use of the discontinuous surface of a segmented DM to create an optical vortex that, by definition, requires a phase discontinuity. The reflective surface allows for generation of vortices of any wavelength and the simple open-loop nature of the controller allows for integer and fractional vortex charge at any wavelength.

CHAPTER 3: MODE PURITY COMPARISON OF OPTICAL VORTICES GENERATED BY A SEGMENTED DEFORMABLE MIRROR AND A MULTILEVEL PHASE PLATE

3.1 SPIRAL PHASE RAMP

The ideal, perfect OV phase profile on a light beam is a linear, continuous, and infinitely smooth phase ramp, like the one represented in Figure 3.1(a).

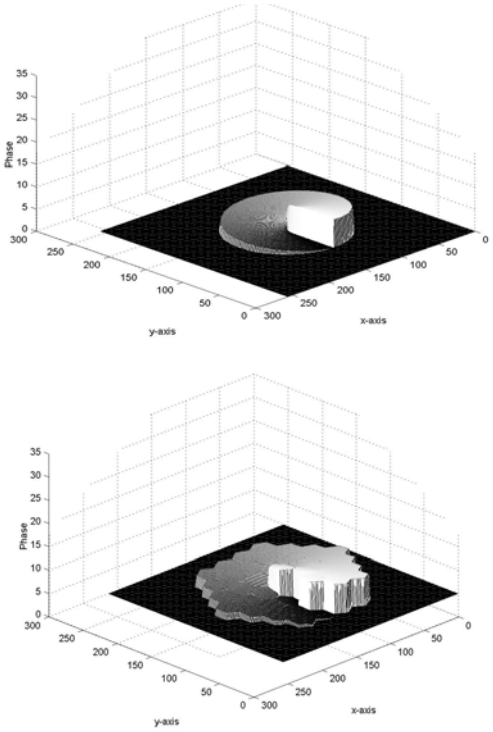

Fig.3.1 Ideal smooth vortex phase ramp 1(a) and DM generated vortex phase ramp 1(b)

Transmissive static phase plates (SPP) are efficient and widely used phase-only optical elements that create a good approximation to the linear spiral phase ramp [12].

The SPPs can be created with continuous phase profiles using fabrication methods like resist melting or reflow. However, these methods are expensive and technically challenging to implement due to large phase depths. In order to ease the fabrication of these micro-optical phase components, the phase topography is usually quantized in N discrete phase levels with equal height (equivalent to $2\pi\ell / N$). This approximates the continuous surface by a staircase profile [9,10,14,15]. The phase profile can also be blazed [4,5,12,13], due to the insensitivity of light to an integer number of 2π phase jumps [1]. The multilevel micro-relieves, with features ranging from submicron to millimeter dimensions, and the possible etching and alignment errors in the photolithographic process, often introduce phase errors in the structure which consequentially deviate the surface from the ideal profile [3]. A 37 segment deformable mirror (DM), based upon an actual device used in experiments and reported elsewhere [16], offers a viable alternative to the SPPs for creating optical vortex beams. The DM is a reflective, reconfigurable, phase only, and polarization- independent device, that approximates the desired linear phase ramp by adjusting tip, tilt, and piston values of the 37 available segments [17] as represented in Figure 3.1(b). The segments have a diameter of 700 μm with $4\mu m$ gaps between them (99 % fill factor). The DM aperture is 3.5 mm in diameter.

This chapter presents a comparison between the phase profile created by the deformable segmented mirror and that of a multilevel, static, phase plate with 16 or 32 discrete levels. The comparison uses vortex mode purity analysis based on circular harmonic decomposition that uses optical vortices with topological charge ranging from 1 to 10.

The vortex mode purity is an indication of the presence of spurious optical vortices in the field.

3.2 CIRCULAR HARMONIC DECOMPOSITION

The circular harmonic decomposition is simply a one-dimensional Fourier series expansion, where the independent variable is the azimuthal angle θ. We used it to analyze the vortex mode purity of a complex field with vortex phase ramp profile produced by a stepped SPP and a field with vortex phase ramp profile generated by the DM. The orthogonal functions used in the decomposition of the field are the orthonormal complex functions $\left\{ e^{im\theta} \right\}_{m=-\infty \; to \; \infty}$. The function $f(r,\theta)$ represents the field profile, represented by a series expansion

$$f(r,\theta) = \sum_{-\infty}^{+\infty} C_m e^{im\theta} \quad . \tag{3.1}$$

The coefficients of the series become

$$C_m = \frac{1}{2\pi} \int_0^{2\pi} f(r,\theta) e^{-im\theta} d\theta \quad . \tag{3.2}$$

The resulting complex coefficients C_m are the amplitudes of vortex modes resulting from the decomposition. A quantized phase SPP acts like a linear kinoform grating structure. It always produces the desired optical vortex with charge ℓ, but it will include extra diffraction orders with unwanted optical vortices of charge other than ℓ.

For the case of the SPP, we can show that by quantizing a field carrying a smooth vortex phase profile, we can generate the weighting factors of the unwanted modes. Mathematically, the mapping of the smooth complex vortex field into a field with a quantized vortex phase can be described by:

$$f(r,\theta) = e^{i\varphi_{quantized}(\theta)} = \sum_{q=1}^{N} e^{i\frac{2\pi}{N}\ell} rect\left[\frac{\theta}{2\pi}N - (q - 1/2)\right] . \quad (3.3)$$

The phasor $e^{i\varphi_{quantized}(\theta)}$ can be synthesized with appropriately weighted vortex modes:

$$e^{i\varphi_{quantized}(\theta)} = \sum_{-\infty}^{+\infty} C_m e^{im\theta} \quad (3.4)$$

where the coefficients C_m are given by the integral

$$C_m = \frac{1}{2\pi}\int_0^{2\pi} e^{i\varphi_{quantized}(\theta)} e^{-im\theta} d\theta \quad (3.5)$$

The resulting coefficients give also the efficiency $\eta_m = |C_m|^2$ of the various vortex modes m :

$$\eta_m \propto \begin{cases} \frac{1}{|m|^2}\sin^2(\frac{m\pi}{N})\frac{\sin^2[\pi(\ell-m)]}{\sin^2[\pi(\ell-m)/N]} & for \quad m = \ell + kN \\ 0 & for \quad m \neq \ell + kN \end{cases} \quad (3.6)$$

which shows that the mode amplitude decreases as $\frac{1}{|m|^2}$ for increasing order m . The second term in the expression is zero for $m = kN$ and third term is indeterminate for $\ell - m = kN$. However, the numerator in the third term goes to zero faster than the denominator and from l' Hopital's rule, in the limit $m \to \ell + kN$, the third term is finite. The logarithmic plot in Figure 3.2 shows the efficiency of the extra vortex modes generated by a step ramp designed for topological charge $\ell = 1$ with N=16 steps (continuous line), and the efficiency for the vortex modes generated by the segmented mirror (segmented line) for the same design charge $\ell = 1$.

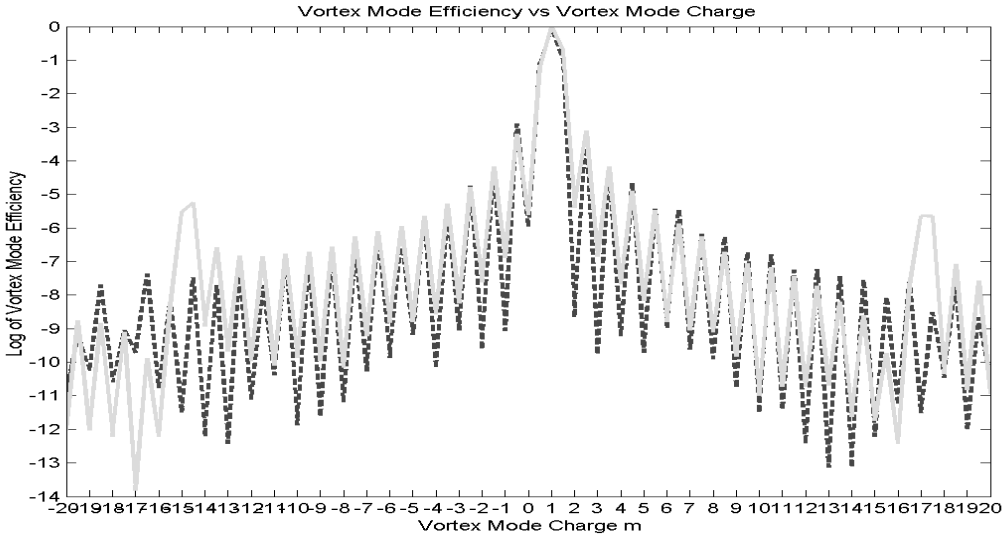

Fig. 3.2 Log plot of mode intensity versus diffraction vortex mode charge for SPP (continuous line) and DM (segmented line)

It is easy to notice how the stepped SPP efficiently reproduces the design mode ℓ (more than 90%) and shows another strong mode of $m = 17$, consistently with Eq. (5). Figure 3.3 illustrates the mode purity versus design topological charge for a 16-step, static, phase spiral ramp versus the phase spiral obtained by using the 37 segment DM. The topological charge on the horizontal axis represents the vortex charge that the device is intended to generate.

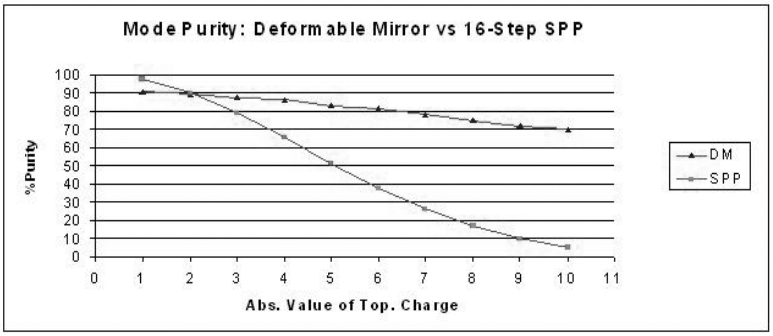

Fig. 3.3 Vortex mode purity versus topological charge for the 16-step SPP and DM generated phase ramp

If the phase ramp was perfectly smooth, the graph would show 100% purity for any design topological charge. The DM and the SPP cannot attain that ideal result, and will generate, therefore, extra vortex modes.

The stepped spiral shows a significant decrease in mode purity with increasing design topological charge after the $m = 2$ value at which both the DM and the 16-step SPP have comparable purity.

This is due to the fact that as the charge increases, the step size increases as well, while the number of discrete steps remains the same. This corresponds to a decrease in angular phase resolution.

Figure 3.4 presents a mode purity analysis between a 32-step SPP and the phase produced by the DM. For optical vortices with topological charge $\ell < 6$, the SPP has slightly superior mode purity, but for higher charges the DM shows a higher purity.

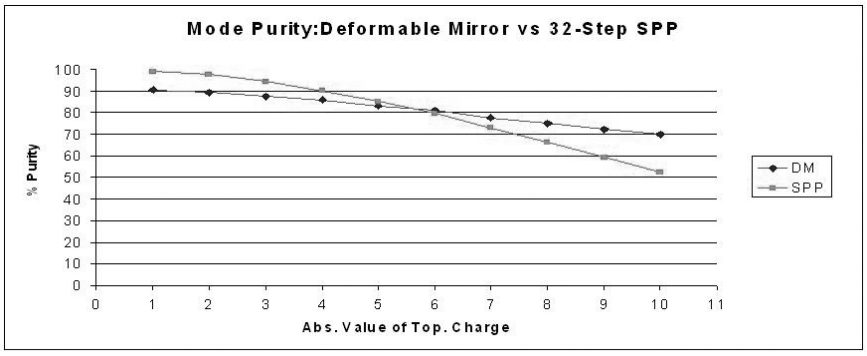

Fig.3.4 Vortex mode purity versus topological charge for the 32-step SPP and DM generated phase ramp

In the case of the stepped SSP, the efficiency clearly increases with the number of the quantization levels. However, microlithographic fabrication puts a limit on the number of discrete phase steps that can actually be realized.

The segmented DM shows more consistent vortex mode purity with increasing topological charge, due to the tilting ability of the segments to better approximate a smooth and continuous surface.

It is interesting to bring to the reader's attention a result first discovered by Molina-Terriza et al. [22]. They showed that net topological charge of a single beam hosting multiple signed vortices is simply the algebraic sum of all the charges. Also they show that the net topological charge of a single beam (that is instead composed of multiple, separate, collinear beams, each carrying a vortex) depends on the relative phase, amplitude, and charge of the individual beams. However, both in the case of the SPP and DM, the beams that carry a vortex charge which is different from the desired design charge, have little effect, in altering the net charge because their amplitude is much smaller.

3.3 SIMULATED INTENSITY AND PHASE AFTER PROPAGATION

We performed a wave-optics simulation of various vortex beams. Figure 3.5(a -f) shows the intensity (a,c,e) and phase (b,d,f) of optical vortices with a 32-step phase ramp.

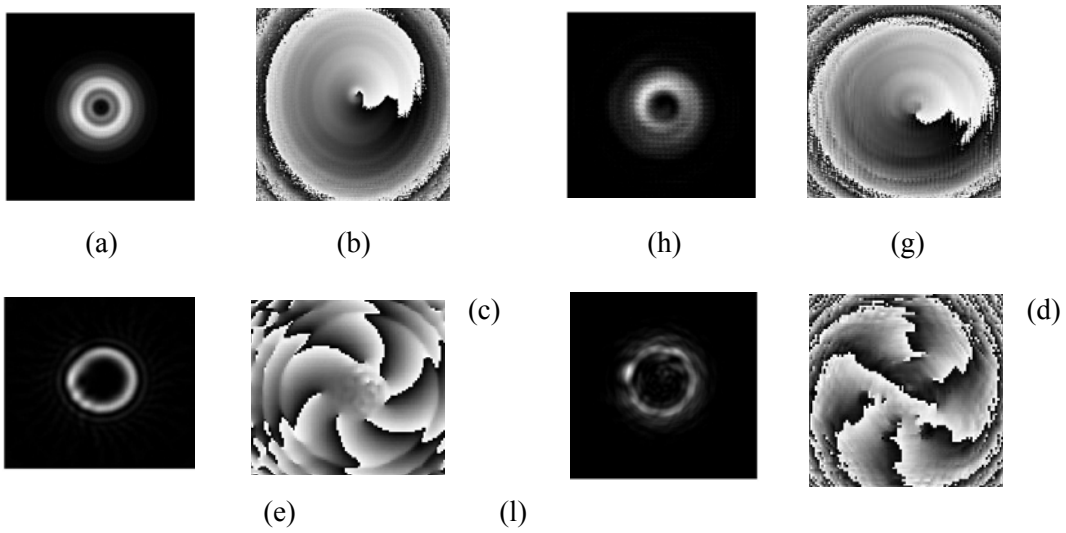

Fig. 3.5 Intensity and phase for vortex beams of charge +1, +6, +10 generated by SPP (5(a-f)). Intensity and phase for vortex beams of charge +1, +6, +10 generated by DM (5(g-n))

Figure 3.5(g-n) shows the intensity (g,i,m) and phase (h,l,n) of optical vortices generated by the DM. The vortices have charges +1, +6 and +10 respectively. The propagation distance is 100 m to reach the far field (Fresnel number <<1), the wavelength is 632.8 *nm* , and the input beam was a uniform amplitude, plane wave with a diameter or 3 mm and the beam at 100 m has a nominal diameter of 27 mm.

The simulation shows that the DM generated phase ramp is effective in creating optical vortices, since both the annular intensity pattern and the phase topography are consistent with the expected theoretical results. The phase figures also show the separation of the vortex into elementary charge 1 vortices. For the fields with topological charge +6 and +10, the separation is recognizable by the fact that the discontinuity phase lines (where

there is a sharp jump from black to white) are not connected and do not meet at a common point.

The intensity and phase of optical vortices generated by the SSP appear less noisy and closer to the ideal results for $\ell < 6$, as expected by Fig. 3.4, due to the asymmetry introduced by the central segment in the DM phase ramp.

For charge +10, the optical vortex generated by the DM, in Figure 3.5(m) and 3.5(n), has intensity and phase profiles very comparable to the intensity and phase profiles of the SPP in Fig. 3.5(e) and 3.5(f).

3.4 CONCLUSIONS

The circular harmonic decomposition and free space propagation simulation were the two methods used to perform a comparison between a segmented DM and a static 16 and 32 step SPP in their ability to generate optical vortices. The DM, because of its reconfigurability and wavelength independence, has higher mode purity than the 16-step SPP for charge $\ell > 2$, and higher mode purity for $\ell > 6$ in the case of the 32-step SPP.

Although the mode purity is high in the case of the DM, the intensity distribution seen from the propagation simulation is irregular, due to the symmetry breaking central segment and jagged phase discontinuity line due to the hexagonal shape of the mirror segments along the line.

It appears that mode purity is sufficient for either device for low charge.

However, for higher charge, there exists the single-wavelength and single charge limitation of the SPP and the broadband capability and variability of the DM.

CHAPTER 4: SPATIAL RANDOM FIELDS AND BISPECTRUM

4.1 RANDOM FIELDS AND SPATIAL COHERENCE

A random signal can be considered as one realization out of the collection of infinite realizations (called an ensemble) of a **random field**, which is a spatial domain equivalent of a time-domain stochastic process, that is indexed by both a spatial variable $\mathbf{r}$ and a time variable t. A random field is a structure describing a phenomenon whose evolution is irregular and unpredictable in space-time with probabilistic properties. There are two types of dynamics: a stochastic one (linear or nonlinear) and chaotic dynamics (typical of some deterministic nonlinear systems). A random field, like a random process, can only be described statistically, since its realizations are different from one another and it is impossible to predict with deterministic certainty their temporal evolution: at every fixed instant of time $t = t_0$ the random field values at different spatial locations $\mathbf{r}$ represent realizations of the random variables forming the random field.

The random field can be viewed as an array of random variables arranged in a certain configuration in space. At later time instants $t > t_0$ new realizations of the random field occur. **Spatial isotropy** and **spatial homogeneity** are two of the main assumptions often made about random spatial fields in order to simplify their statistical analysis. Spatial isotropy implies that there is not a preferential spatial direction in the random

field: statistics along different directions are the same. Spatial homogeneity states instead that the local statistics are the same everywhere, at any spatial position in the random field: the mean, variance, joint moments, and all other statistical quantities are not a function of $\mathbf{r}$. All the finite dimensional distribution functions defining the process remain the same if shifted anywhere in the spatial Cartesian domain. Isotropic, homogeneous, scalar random fields, where the random field value at a specific space location represents the electric (magnetic) field as a random variable, are the type of random fields discussed in this dissertation. The probabilistic structure of random fields is determined by the correlation (coherence) functions of various order. The coherence functions investigate and measure the statistical relationship existing between the values of the random wavefield at multiple different spatial locations $\mathbf{r_1},\mathbf{r_2},\mathbf{r_3},....,\mathbf{r_n}$ and multiple different instants in time $t_1,t_2,t_3,...,t_n$. In the case the field observations are made at a fixed single spatial location, i.e. $\mathbf{r_1} = \mathbf{r_2} = \mathbf{r_3} = ... = \mathbf{r_n}$, but at different instants of time, the ``**temporal coherence**'' properties of the optical wavefield are measured and explored. The property of homogeneity allows us to freely choose any spatial location $\mathbf{r}$ for our observations, since the statistical properties are independent of spatial position $\mathbf{r}$ (different spatial locations have the same statistical characteristics). If the optical wavefield is instead probed at multiple different spatial points ``simultaneously'', at the same instant $t$, the ``**spatial coherence**'' properties of optical wavefield are inspected. The topics treated in this thesis focus on the spatial coherence of optical fields.

4.2 SPATIAL CORRELATION FUNCTIONS

Correlation (coherence) functions are simply a different name for the ``**joint'' central moments,** which are functions that specify a complex-valued random field. The joint central moments m_ψ^r of order r are obtained selecting a number $r \geq 2$ of centered (zero mean) random variables $\psi(\mathbf{r_1}),\psi(\mathbf{r_2}),\psi(\mathbf{r_3}),...$ in the random field. The vector variable $\mathbf{r}$ represents the two-dimensional Cartesian position vector (x, y) in a plane at arbitrary distance z. Denoting the field random variables $\psi(\mathbf{r_1}) = \psi_1$, $\psi(\mathbf{r_2}) = \psi_2 ...$, $E[\cdot]$ as the expectation operator, $f(\psi_1,\psi_2,...;\mathbf{r_1},\mathbf{r_2},...)$ as the joint probability distribution function, the joint moments m_ψ^r of order $r = 1,2,3$ (studied in this dissertation) are defined as ensemble averages which are averaging operations along the ensemble of the field realizations. The first moment is defined as

$$m_\psi^1(\mathbf{r_1}) = E[\psi_1] = \int_{-\infty}^{\infty} \psi_1 f(\psi_1;\mathbf{r_1}) d\psi_1 = E[\psi(\mathbf{r})] = lim_{N\to\infty} \frac{1}{N}\sum_{i=1}^{N} \psi(\mathbf{r}) \qquad (4.1)$$

In practice (experiments and computer simulations) the number N of realizations is finite and only estimation (approximation) of the moments can be obtained. The 2nd- and 3rd moments follow analogous definitions:

$$m_\psi^2(\mathbf{r_1},\mathbf{r_2}) = E[\psi_1\psi_1^*] = \int_{-\infty}^{\infty} \psi_1\psi_2^* f(\psi_1,\psi_2;\mathbf{r_1},\mathbf{r_2}) d\psi_1 d\psi_2 \qquad (4.2)$$

$$m_\psi^3(\mathbf{r_1},\mathbf{r_2},\mathbf{r_3}) = E[\psi_1()\psi_2\psi_3^*] = \int_{-\infty}^{\infty} \psi_1\psi_2\psi_3^* f(\psi_!,\psi_2,\psi_3;\mathbf{r_1},\mathbf{r_2},\mathbf{r_3}) d\psi_1 d\psi_2 d\psi_3 \qquad (4.3)$$

The complex conjugation * can be applied either on one or two entries of the triple product in $m_\psi^3(\mathbf{r_1},\mathbf{r_2},\mathbf{r_3})$. The choice is purely academic. The resulting moments will turn out to be different functions containing the same information. Higher order moments

($r \geq 4$) can also be defined as the ensemble averages of the products of four or more random field variables.

If a field is completely coherent the various autocorrelation functions factorize into a product of the fields at separate spatial points. A "perfectly" coherent field can be defined as one whose autocorrelation functions of all imaginable orders can be factored. Closely related to joint moments m_ψ^r are the **joint cumulant functions** κ_ψ^r or order r. For a zero-mean complex random field ψ the joint cumulant functions κ_ψ^r are linear combinations of joint moments m_ψ^r. Limiting out attention to the order $r = 1,2,3$ the joint cumulant-joint moments relations are

$$\kappa_\psi^1(\mathbf{r_1}) = m_\psi^1(\mathbf{r_1}) \tag{4.4}$$

$$\kappa_\psi^2(\mathbf{r_1},\mathbf{r_2}) = m_\psi^2(\mathbf{r_1},\mathbf{r_2}) \tag{4.5}$$

$$\kappa_\psi^3(\mathbf{r_1},\mathbf{r_2},\mathbf{r_3}) = m_\psi^2(\mathbf{r_1},\mathbf{r_2},\mathbf{r_3}) \tag{4.6}$$

A recursion relation can be used in order to calculate higher order cumulants from central moments. Cumulants represent an alternative way to describe a random field structure [25,33,34,41]. Because of the postulated spatial homogeneity of the random fields studied in this thesis, all the joint moments and joint cumulants are invariant upon any translation in space, i.e. they are space-independent and become only function of position difference vectors:

$$\kappa_\psi^1(\mathbf{r_1}) = \kappa_\psi^1 = constant \tag{4.7}$$

$$\kappa_\psi^2(\mathbf{r_1},\mathbf{r_2}) = \kappa_\psi^2(\Delta\mathbf{r}') \tag{4.8}$$

$$\kappa_\psi^3(\mathbf{r_1},\mathbf{r_2},\mathbf{r_3}) = \kappa_\psi^3(\Delta\mathbf{r}',\Delta\mathbf{r}'') \tag{4.9}$$

I chose to use joint cumulants for three reasons: 1) The cumulants of a random field that sum of statistically ``independent'' random fields is the sum of the cumulants of the individual random fields [25,31]; 2) Homogeneous, additive noise random fields with symmetric marginal probability distribution functions (homogeneous Laplacian, Gaussian, uniform, Bernoulli Gaussian are symmetrically distributed random fields) have all their joint moments m_ψ^r and joint cumulants κ_ψ^r with order r being an odd number are automatically zero. For a white or colored Gaussian random field all the cumulants of order $r > 2$ (odd or even) are equal to zero. This implies that any Gaussian random field is completely characterized by its first two central moments (or central cumulants). Cumulants are a useful method to estimate the degree of departure from Gaussianity of a random field.

3) White noise has joint cumulants that are multidimensional Dirac impulse functions. The polyspectra of this type of noise are multidimensionally flat.

4.3 GAUSSIANITY AND 2ND ORDER STATISTICS

To gain complete knowledge of a random field we need to know all its finite probabilistic distributions functions [31,32,35]. They could be approximately and experimentally calculated but the effort would be immense and unpractical. We often restrict the analysis to the simplest characteristics of the multidimensional distributions.The mean describes the coarsest properties of the random process. Correlation theory, also called 2nd order statistics, is based on the study of only those properties extracted by the first and second moments. It is important to realize that the mean value and the second moment do not specify the random process uniquely. Therefore 2nd order statistics cannot replace a complete theory of random field which

uses multi-dimensional distributions. However, if the random field is Gaussian all the finite-dimensional distribution functions are Gaussian and specified completely by the the first two moments. The classical assumption of Gaussianity justifies the use of second order techniques which are well understood and easy to work with [32, 34]. The realizations of homogeneous, zero-mean random field $\psi(\mathbf{r},p)$ are wavefields with infinite spatial extent (due to spatial homogeneity). Such realizations do not admit a regular Fourier transform (they are not absolutely integrable) or a Fourier series (they are not periodic). There are two basic representations associated with a homogeneous random field with zero mean. One of them is called the Wold-Cramer representation using the Fourier Stieltjes. The Fourier Stieltjes is still a Fourier expansion but more general thant the Fourier transform or the Fourier series [30,39,40]. Using the Fourier Stieltjes integral the random field is expressed as the stochastic integral (defined in the mean square sense)

$$\psi(\mathbf{r}) = \int_{-\infty}^{\infty} e^{i\mathbf{k}\cdot\mathbf{r}} dZ(\mathbf{k}) \tag{4.10}$$

where $\mathbf{k}$ represents the ``transverse" two-dimensional, spatial wavevector. The function $Z(\mathbf{k})$ is a complex random process with uncorrelated increments and $E[dZ(\mathbf{k})] = 0$ for all $\mathbf{k}$. This representation is founded on harmonic analysis and expresses the homogeneous random field $\psi(\mathbf{r})$ as a superposition of sinusoidal signals (plane waves) of different wave-vector magnitudes and travelling directions. For any fixed plane wave the amplitude and relative phase angle are constant in a single realization but vary stochastically from one realization to the next. The Cramer integral is in principle the same as generalized Fourier transform. The problem is that the realizations of a homogeneous random field are infinite in extent but not periodic, so that Fourier series or the regular Fourier integral cannot be applied. Even if it were possible to Fourier

transform each realization p (in real life we deal with finite size realizations that are Fourier transformable), a different complex Fourier spectrum $F_p(\mathbf{k})$ would be obtained for each p. Emsemble averaging all the amplitude spectra $|F_p(\mathbf{k})|$ and phase spectra $\angle F_p(\mathbf{k})$ would simply return a zero average amplitude and phase spectra. If the averaging procedure along the ensemble is instead applied to the magnitude square spectrum $|F_p(\mathbf{k})|^2$ of the realizations, a function called the Power Spectral density $S(\mathbf{k})$ is obtained:

$$S(\mathbf{k}) = lim_{dA\to\infty} E[\frac{|F_p(\mathbf{k})|^2}{|d\mathbf{A}|}] \tag{4.11}$$

where $|d\mathbf{A}|$ is an elementary surface area of the random field. The power spectral density $S(\mathbf{k})$ is **always** a real-valued, positive function. The term `power` is used in a generalized sense, indicating the expected squared value of the members of the ensemble. The other alternative path to describe a homogeneous random field is via the second order joint moment $m_\psi^2(\Delta\mathbf{r}')$, also called the 2-point spatial autocorrelation function $R(\Delta\mathbf{r}')$ in optics . Using the Cramer representation we can derive a spectral representation of $R(\Delta\mathbf{r}')$:

$$R(\Delta\mathbf{r}') = E[\psi(\mathbf{r})\psi^*(\mathbf{r}+\Delta\mathbf{r}')] = \int_{-\infty}^{\infty} e^{+j(\mathbf{k_1}-\mathbf{k_2})\cdot\mathbf{r}} e^{+j(\mathbf{k}\cdot\Delta\mathbf{r}')} E[dU(\mathbf{k_1})dU^*(\mathbf{k_2})] \tag{4.12}$$

Since the function $R(\Delta\mathbf{r}')$ is only a function of $\Delta\mathbf{r}'$ (homogeneous field) and independent of $\mathbf{r}$, any contribution to the integral is zero when $\mathbf{k_1} \neq \mathbf{k_2}$ leading to

$$E[dU(\mathbf{k_1})dU^*(\mathbf{k_2})] = S(\mathbf{k_1})\delta(\mathbf{k_1}-\mathbf{k_2})d\mathbf{k} \tag{4.13}$$

which means that two different spectral components with $\mathbf{k}_1$ and $\mathbf{k}_2$ wave vectors are ``uncorrelated''. The function $S(\mathbf{k})$ is called the power spectral density function and expresses the power (variance) distribution of the random field in spatial frequency domain, i.e. the contribution to the variance from the component $U(\mathbf{k})$ having frequencies in the range $\mathbf{k} + d\mathbf{k}$. Using the new definition of power spectral density $S(\mathbf{k})$ the autocorrelation integral $R(\Delta\mathbf{r}')$ becomes

$$R(\Delta\mathbf{r}') = \int_{-\infty}^{\infty} S(\mathbf{k}) e^{+j(\mathbf{k}\cdot\Delta\mathbf{r}')} d\mathbf{k} \tag{4.14}$$

The function $S(\mathbf{k})$ and the second order joint moment $R(\Delta\mathbf{r}')$, form an exact Fourier pair, leading to

$$S(\mathbf{k}) = \frac{1}{(2\pi)^2} \int_{-\infty}^{\infty} R(\Delta\mathbf{r}') e^{-j(\mathbf{k}\cdot\Delta\mathbf{r}')} d(\Delta\mathbf{r}') \tag{4.15}$$

The power spectral density $S(\mathbf{k})$ and the 2-point autocorrelation function $R(\Delta\mathbf{r}')$ contain the same information in two reciprocal domains. $S(\mathbf{k})$ provides information on how the power of the random field is distributed among the composing spatial frequencies $\mathbf{k}$:

$$variance = E[\psi(\mathbf{r})^2] = R(\Delta\mathbf{r}' = 0) = \int_{-\infty}^{\infty} S(\mathbf{k}) d\mathbf{k} \tag{4.16}$$

It does not provide any information regarding the potentially existing statistical phase relations between the various spatial frequencies $\mathbf{k}$. The power spectral density $S(\mathbf{k})$ is said to be **phase blind** [42,43,49]. Conversely, the autocorrelation function $R(\Delta\mathbf{r}')$ measures ONLY the degree of linear dependence, called correlation, between a random field and itself. A zero correlation does not imply independence but full independence does imply uncorrelatedness. The autocorrelation function and the power spectral density

are represent 2nd order statistics which characterize only partially a stochastic random field. Higher order statistics like the 3rd or higher order cumulants and their spectra (called polyspectra) can be helpful in order to achieve a more complete knowledge of a random field. As a reminder, only if the homogeneous random field is Gaussian (its joint pdfs of any order are Gaussian), 2nd order statistics are sufficient. All higher order moments and cumulants are derivable from the mean and autocorrelation function. The powerful **central limit theorem** (CLT) states that any stochastic physical quantity produced by the cumulative effect of many independent random variables will approximatelly have Gaussian statistics, regardless of the pdfs of the starting random variables (the pdf of the resulting random variable is the convolution of the pdfs of the summed random variables and will asymptotically tend to Gaussian shape). Invoking the central limit theorem automatically leads to Gaussian statistics that are entirely measured by 2nd order statistics (autocorrelation and spectrum). Gaussian random fields can only exhibit one type of statistical dependence (if any), which is linear dependence (called correlation) and linear dependence is evaluated by the 2-point autocorrelation function $R(\Delta\mathbf{r}')$. However not every physical, stochastic phenomenon is Gaussian in nature. Strong turbulence is an example. As mentioned above, correlation is a first order type of statistical dependence. Full statistical independence is much stronger than uncorrelatedness. Multiple random variables $a,b,c,...$ are statistically independent if their joint density can be factorized into the product of marginal densities:

$$p_{a,b,c,...}(a,b,c,..) = p_a(a)p_b(b)p_c(c)... \tag{4.17}$$

This definition of independence is equivalent to $E[g(a)f(b)h(c)....] = E[g(a)]E[f(b)]E[h(c)]...$ where $g,f,h,...$ are any absolutely

integrable functions of $a,b,c,...$ A Gaussian homogeneous random field will be composed of complex sinusoids whose amplitudes and phases are random variables that are uncorrelated and also independent since uncorrelatedness=independence only in the Gaussian case. Non-Gaussian homogeneous random fields will still have uncorrelated spectral components but not necessarily independent. The third order cumulant is instead able shine light on the presence of dependent spectral components in the random field.

4.4 BISPECTRUM

The Fourier transforms of the joint cumulant functions of random fields are multidimensional spectra called polyspectra [21]. I concentrated only on the 3rd order joint cumulant $\kappa_{\psi}^{3}(\mathbf{r_1},\mathbf{r_2},\mathbf{r_3}) = R(\mathbf{r_1},\mathbf{r_2},\mathbf{r_3}) = E[\psi^{*}(\mathbf{r_1})\psi(\mathbf{r_2})\psi(\mathbf{r_3})]$ which is a function of three independent spatial positions $\mathbf{r_1},\mathbf{r_2},\mathbf{r_3}$ if the random field is spatially non-homogeneous. In the special case of spatial homogeneity, $R(\mathbf{r_1},\mathbf{r_2},\mathbf{r_3}) \rightarrow R(\Delta\mathbf{r}',\Delta\mathbf{r}'') = E[\psi^{*}(\mathbf{r_1})\psi(\mathbf{r}+\Delta\mathbf{r}')\psi(\mathbf{r}+\Delta\mathbf{r}'')]$, also called the 3-point correlation function, since it quantifies the self-correlation of the field at three different spatial points [25,26,27,28,29]. For a complex-valued random field $\psi(\mathbf{r})$ the symmetry property of the third-order cumulant is $R(\Delta\mathbf{r}',\Delta\mathbf{r}'') = R(\Delta\mathbf{r}'',\Delta\mathbf{r}')$, giving two regions of symmetry separated by the line $\Delta\mathbf{r}' = \Delta\mathbf{r}''$ (half plane symmetry) [37,49]. A real-valued random field has instead six regions of symmetry for the third-order cumulant. The 3-point autocorrelation function, different from the two-point autocorrelation, is able to detect statistical dependence other than correlation in a random field. The Fourier transform of $R(\Delta\mathbf{r}',\Delta\mathbf{r}'')$ is called the bispectrum $B(\mathbf{k_1},\mathbf{k_2})$. There are $2^3 = 8$ different versions of the 3-point autocorrelation function depending on which entry(s) of the triple

product are complex conjugated. Different triple product versions give completely different bispectral functions $B(\mathbf{k_1},\mathbf{k_2})$. I chose to apply the complex conjugation only the first entry: $R(\Delta\mathbf{r}',\Delta\mathbf{r}'') = E[\psi^*(\mathbf{r}_1)\psi(\mathbf{r}+\Delta\mathbf{r}')\psi(\mathbf{r}+\Delta\mathbf{r}'')]$. An effective way to undertand the meaning and interpretation of the bispectrum function $B(\mathbf{k_1},\mathbf{k_2})$ is to follow the steps that lead to the construction of the triple autocorrelation function $R(\Delta\mathbf{r}',\Delta\mathbf{r}'')$. The random field at one spatial point $\mathbf{r}$ is given by

$$\psi(\mathbf{r}) = \int_{-\infty}^{\infty} e^{i\mathbf{k_1}\cdot\mathbf{r}}\, dU(\mathbf{k_1}) \tag{4.18}$$

The fields at a two different shifted spatial points $(\mathbf{r}+\Delta\mathbf{r}')$ and $(\mathbf{r}+\Delta\mathbf{r}'')$ are

$$\psi(\mathbf{r}+\Delta\mathbf{r}') = \int_{-\infty}^{\infty} e^{i\mathbf{k_2}\cdot\mathbf{r}} e^{i\mathbf{k_2}\cdot\Delta\mathbf{r}'}\, dU(\mathbf{k_2}) \tag{4.19}$$

$$\psi(\mathbf{r}+\Delta\mathbf{r}'') = \int_{-\infty}^{\infty} e^{i\mathbf{k_3}\cdot\mathbf{r}} e^{i\mathbf{k_3}\cdot\Delta\mathbf{r}''}\, dU(\mathbf{k_3}) \tag{4.20}$$

The three vector variables $\mathbf{k_1},\mathbf{k_2},\mathbf{k_3}$ all represent the same physical quantity, the spatial wave-vector $\mathbf{k}$ (spatial frequency). Giving them different names will serve us to comprehend the significance of the statistical dependence between different values of the wave-vector $\mathbf{k}$. The ``unaveraged'' triple product is given by

$$\psi^*(\mathbf{r})\psi(\mathbf{r}+\Delta\mathbf{r}')\psi(\mathbf{r}+\Delta\mathbf{r}'') = \int_{-\infty}^{\infty} e^{i(-\mathbf{k_1}+\mathbf{k_2}+\mathbf{k_3})\cdot\mathbf{r}} e^{i\mathbf{k_2}\cdot\Delta\mathbf{r}'} e^{i\mathbf{k_3}\cdot\Delta\mathbf{r}''}\, d^*U(\mathbf{k}_1)dU(\mathbf{k_2})dU(\mathbf{k_3}) \tag{4.21}$$

Taking the expectation of the product results in 3-point autocorrelation

$$R(\Delta\mathbf{r}',\Delta\mathbf{r}'') = E[\psi^*(\mathbf{r})\psi(\mathbf{r}+\Delta\mathbf{r}')\psi(\mathbf{r}+\Delta\mathbf{r}'')] = \int_{-\infty}^{\infty} e^{i(-\mathbf{k_1}+\mathbf{k_2}+\mathbf{k_3})\cdot\mathbf{r}} e^{i\mathbf{k_2}\cdot\Delta\mathbf{r}'} e^{i\mathbf{k_3}\cdot\Delta\mathbf{r}''} E[d^*U(\mathbf{k}_1)dU(\mathbf{k_2})dU(\mathbf{k_3})] \tag{4.22}$$

We should notice that since the random field is homogeneous, the lefthand side must be independent of $\mathbf{r}$. That forces the righhand side to be independent of $\mathbf{r}$. Only triads of

wave-vectors $\mathbf{k}_1,\mathbf{k}_2,\mathbf{k}_3$ related by the relation $(-\mathbf{k}_1+\mathbf{k}_2+\mathbf{k}_3)=\mathbf{0}$, meaning that $\mathbf{k}_1=\mathbf{k}_2+\mathbf{k}_3$, will contribute to a nonzero 3-point correlation. This leads to

$$E[d^*U(\mathbf{k}_1=\mathbf{k}_2+\mathbf{k}_3)dU(\mathbf{k}_2)dU(\mathbf{k}_3)]=B(\mathbf{k}_2,\mathbf{k}_3)\delta(-\mathbf{k}_1+\mathbf{k}_2+\mathbf{k}_3) \qquad (4.23)$$

Clearly the subscripts 1,2,3 are arbitrary and we can re-write the formula as $\mathbf{k}_3=\mathbf{k}_1+\mathbf{k}_2$.

$$E[d^*U(\mathbf{k}_3=\mathbf{k}_1+\mathbf{k}_2)dU(\mathbf{k}_1)dU(\mathbf{k}_2)]=B(\mathbf{k}_1,\mathbf{k}_2)\delta(\mathbf{k}_1+\mathbf{k}_2-\mathbf{k}_3) \qquad (4.24)$$

and rearranging the order of the product of three numbers the product does not change

$$E[dU(\mathbf{k}_1)dU(\mathbf{k}_2)d^*U(\mathbf{k}_3=\mathbf{k}_1+\mathbf{k}_2)]=B(\mathbf{k}_1,\mathbf{k}_2)\delta(\mathbf{k}_1+\mathbf{k}_2-\mathbf{k}_3) \qquad (4.25)$$

Note also that if the random process is real-valued $dU(-\mathbf{k})=d^*U(\mathbf{k})$, then

$$E[dU(\mathbf{k}_1)dU(\mathbf{k}_2)dU(\mathbf{k}_3=-\mathbf{k}_1-\mathbf{k}_2)]=B(\mathbf{k}_1,\mathbf{k}_2)\delta(\mathbf{k}_1+\mathbf{k}_2-\mathbf{k}_3) \qquad (4.26)$$

and the bispectrum is nonzero for three frequencies that sum to zero: $\mathbf{k}_1+\mathbf{k}_2+\mathbf{k}_3=\mathbf{k}_1+\mathbf{k}_2+(-\mathbf{k}_1-\mathbf{k}_2)=\mathbf{0}$. Finally the triple autocorrelation becomes the inverse Fourier transform of bispectrum $B(\mathbf{k}_1,\mathbf{k}_2)$:

$$R(\Delta\mathbf{r}',\Delta\mathbf{r}'')=E[\psi^*(\mathbf{r})\psi(\mathbf{r}+\Delta\mathbf{r}')\psi(\mathbf{r}+\Delta\mathbf{r}'')]=\int_{-\infty}^{\infty}B(\mathbf{k}_1,\mathbf{k}_2)e^{i\mathbf{k}_2\cdot\Delta\mathbf{r}'}e^{i\mathbf{k}_3\cdot\Delta\mathbf{r}''}d\Delta\mathbf{k}_1d\Delta\mathbf{k}_2 \qquad (4.27)$$

Integration of the bispectrum for $\Delta\mathbf{r}'=0,\Delta\mathbf{r}''=0$ give the marginal skewness of the homogeneous random process $\psi(\mathbf{r})$:

$$skewness=E[\psi(\mathbf{r})^3]=R(\Delta\mathbf{r}'=0,\Delta\mathbf{r}''=0)=\int_{-\infty}^{\infty}B(\mathbf{k}_1,\mathbf{k}_2)d\mathbf{k}_1d\mathbf{k}_2 \qquad (4.28)$$

Like the third-order cumulant, the bispectrum has half-symmetry in the plane $\mathbf{k}_1,\mathbf{k}_2$: $B(\mathbf{k}_1,\mathbf{k}_2)=B(\mathbf{k}_2,\mathbf{k}_1)$. If the random field were real-valued, twelve regions of symmetry would be available.

Usually, instead of working with the bispectrum $B(\mathbf{k_1},\mathbf{k_2})$ it is better its normalized version $b(\mathbf{k_1},\mathbf{k_2})$:

$$b(\mathbf{k}_1,\mathbf{k}_2)=\frac{|B(\mathbf{k}_1,\mathbf{k}_2)|}{\sqrt{P(\mathbf{k}_1)P(\mathbf{k}_2)P(\mathbf{k}_1+\mathbf{k}_2)}} \tag{4.29}$$

called the bicoherence function.

If the stochastic distribution function $U(\mathbf{k})$ describing a random process is continuous and differentiable, then $dU(\mathbf{k}) = Z(\mathbf{k})d\mathbf{k}$. The function $Z(\mathbf{k})$ represents the complex-valued amplitude of each Fourier component composing the random field: is represented as $Z(\mathbf{k}) = A(\mathbf{k})e^{i\theta(\mathbf{k})}$. A nonzero bispectrum function $B(\mathbf{k_1},\mathbf{k_2})$ indicates the existence of a joint statistical distribution function for the phases $\theta(\mathbf{k})$ and amplitudes $A(\mathbf{k})$. In Gaussian random fields the Fourier components are independent and both the phases and amplitudes are random without any interelation: the amplitudes $A(\mathbf{k})$ are Rayleigh distributed, and $\theta(\mathbf{k})$ are completely random with respect to each other [38]. In non-Gaussian fields, the phases $\theta_1,\theta_2,\theta_3$ are **not** completely random and are therefore correlated. However their correlation is not pairwise and is only properly captured by the simultaneous distribution of the three phase angles $\theta_1,\theta_2,\theta_3$. An interesting article by Matsubara discusses the issue in wide detail [47,48]. As the integral of the spectrum $S(\mathbf{k})$ gives the variance $E[\psi(\mathbf{r})^2] = E[\psi^2]$ of random homogeneous fields, the integral of the bispectrum $B(\mathbf{k_1},\mathbf{k_2})$ decomposes the random field ``skewness'' in $\mathbf{k}$ space. A Gaussian random field has null skewness so a non-zero skewness is an indication of departure from Gaussianity and tells us that the random process is non-Gaussian [36,37,38].

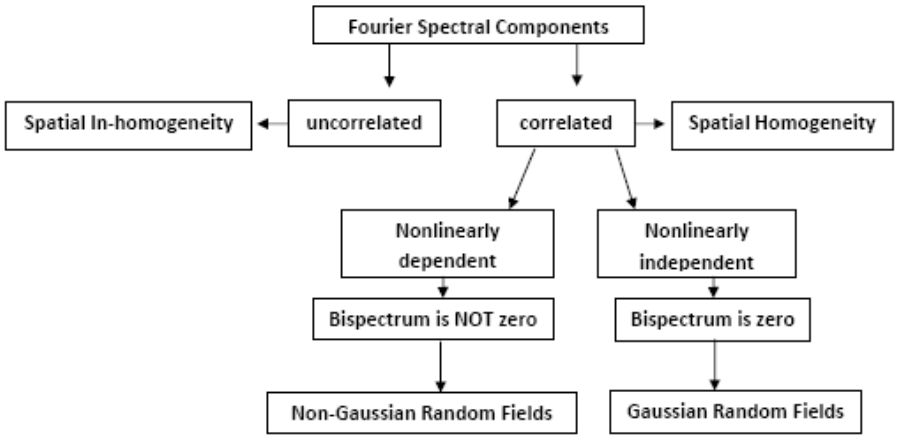

Fig. 4.1 Schematic chart illustrating how spectral components relate to different types of random fields

4.5 QUADRATIC PHASE COUPLING

The statistical dependence among the phases and/or amplitudes of the Fourier components of a random fields with nonzero bispectrum can assume different functional forms [47,48]. A special and particular type of dependence among random phases is the ``quadratic phase coupling'' commonly generated by quadratic nonlinear systems. In the case of quadratic phase coupling the bispectrum $B(\mathbf{k_1},\mathbf{k_2}) \neq 0$ when three Fourier components have wavevectors $\mathbf{k_1}, \mathbf{k_2}, \mathbf{k_3}$ and random phase angles $\theta_1, \theta_2, \theta_3$ that satisfy the following two resonant conditions [35]:

$$\text{a) } \mathbf{k_3} = \mathbf{k_1} + \mathbf{k_2} \tag{4.30}$$

$$\text{b) } \theta_3 = \theta_1 + \theta_2 \tag{4.31}$$

The second equation forces a linear dependence between the three random phases, typically present in random fields generated by nonlinear quadratic systems.

The bispectrum $B(\mathbf{k_1},\mathbf{k_2})$ inspects any triad of spectral components fullfilling the two resonant conditions a) and b).

Example: A random field ψ is the sum of three harmonic random process: $\psi = A_1 e^{i\phi_1} + A_2 e^{i\phi_2} + A_3 e^{i\phi_3}$, where $\phi_n = (\mathbf{k}_n \cdot \mathbf{r} + \theta_n)$ is the total phase of each harmonic. The coefficients A_1, A_2, A_3 are constants while the phases $\theta_1, \theta_2, \theta_3$ are pairwise uncorrelated random variables changing unpredicatably over the ensemble but constant in every single realization of the random field. The bispectrum of ψ is equal to

$$B(\mathbf{k_1},\mathbf{k_2}) = E[A_1\delta(\mathbf{k}-\mathbf{k}_1)A_2\delta(\mathbf{k}-\mathbf{k}_2)A_3\delta(\mathbf{k}-\mathbf{k}_3)e^{i(\theta_1+\theta_2-\theta_3)}] =$$

$$= A_1A_2A_3E[\delta(\mathbf{k}-\mathbf{k}_1)A_2\delta(\mathbf{k}-\mathbf{k}_2)A_3\delta(\mathbf{k}-\mathbf{k}_3)e^{i(\theta_1+\theta_2-\theta_3)}] =$$

$$= A_1A_2A_3\delta(\mathbf{k_3}-\mathbf{k_2}-\mathbf{k_1})E[e^{i(\theta_1+\theta_2-\theta_3)}] \qquad (4.32)$$

Its value is nonzero when $\mathbf{k_3}-\mathbf{k_2}-\mathbf{k_1}=0$ and $E[e^{i(\theta_1+\theta_2-\theta_3)}]\neq 0$ which happens when the random variable $\theta_1+\theta_2-\theta_3 = any\ constant$. Quadratic nonlinear systems create a quadratic phase coupling with $\theta_1+\theta_2-\theta_3=0$.

To further clarify the concept of quadratic phase coupling Figure 4. shows the normalized bispectrum for two one-dimensional complex harmonics with random phases in fixed relation.Their wave vectors are $\mathbf{k_1} = (k_{1x},0) = (50,0)$ and $\mathbf{k}_2 = (k_{2x},0) = (30,0)$ respectively.

The two peaks of magnitude 1 indicate the perfect quadratic phase coupling between the two harmonics. Either one of the two peaks is redundant: both peaks suggest that there is phase coupling between two one dimensional wavevector, one of magnitude 30 rad/m and the other 50 rad/m or vice versa.

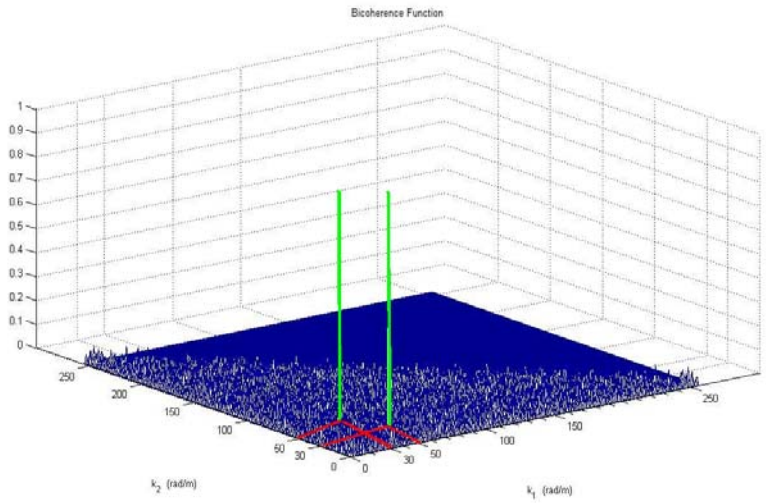

Fig. 4.2 Normalized bispectrum for a set of two harmonic in quadratic phase coupling

In the case of no phase coupling the normalized bispectrum would be zero everywhere:

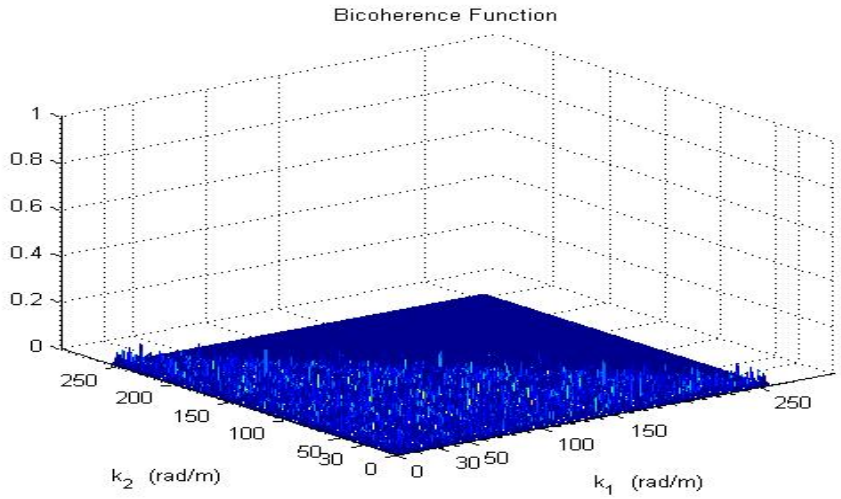

Fig. 4.3 Zero normalized bispectrum for uncoupled harmonics

4.6 LINEAR FILTERING OF RANDOM FIELDS BY SPACE-INVARIANT SYSTEMS

A 2-dimensional linear space invariant (LSI) system $\mathbb{T}\{\cdot\}$ is a mathematical linear operator that describes the action of a physical system on some input n-dimensional signal to generate an output signal:

$$\mathbb{T}\{X\}(\mathbf{r}) = Y(\mathbf{r}) \tag{4.33}$$

where X is the input signal, Y the output signal and $\mathbf{r} = (x,y)$ the Cartesian position vector[25,39,46]. LSI systems, like any linear system, can be fully characterized by its impulse response function $h(\mathbf{r})$, which the the output of the system when driven by a Dirac impulse $X(\mathbf{r}) = \delta(\mathbf{r}) = \delta_0$ located at the spatial coordinates $\mathbf{r_0} = \mathbf{0}$:

$$\mathbb{T}\{\delta_0\}(\mathbf{r}) = h(\mathbf{r}) \tag{4.34}$$

The spatial invariance property (also called isoplanatism) of LSI systems derives from the fact that a spatial translation of the input impulse $\delta(x,y)$ to any arbitrary location $\mathbf{r} = \mathbf{r_0}$ ($\forall x,y \in \mathbb{R}$) will have the system generate a response function that is functionally identical (hence the invariance) to the response to the δ input excitation located at the origin $\mathbf{r_0} = \mathbf{0}$, just translated:

$$\mathbb{T}\{\delta_{\mathbf{r_0}}\}(\mathbf{r}) = h(\mathbf{r} - \mathbf{r_0}) \tag{4.35}$$

When the input to the system is not a δ function but an arbitrary signal, the output of the system is obtained by the **convolution integra**l:

$$Y(\mathbf{r}) = (X \otimes h)(\mathbf{r}) =$$

$$= \int_{-\infty}^{\infty} X(\mathbf{r_0}) h(\mathbf{r} - \mathbf{r_0}) d\mathbf{r_0} = \int_{-\infty}^{\infty} h(\mathbf{r_0}) X(\mathbf{r} - \mathbf{r_0}) d\mathbf{r_0} \tag{4.36}$$

4.6.1 FILTERING THE AUTOCORRELATION FUNCTION

Whenever a random field $\psi_{in}(\mathbf{r})$ is applied as the input to a linear space-invariant system $\mathbb{T}\{\cdot\}$ with complex-valued impulse response $h(\mathbf{r})$, the system produces a random process $\psi_{out}(\mathbf{r})$ as the output:

$$\mathbb{T}\{\psi_{in}\}(\mathbf{r}) = \psi_{out}(\mathbf{r}) \tag{4.37}$$

If $R_{in}(\Delta\mathbf{r})$ is the autocorrelation of the input random field $\psi_{in}(\mathbf{r})$, the autocorrelation of the output random field is given by

$$R_{out}(\Delta\mathbf{r}) = E[\psi^*_{out}(\mathbf{r})\psi_{out}(\mathbf{r}+\Delta\mathbf{r})] =$$

$$\int_{-\infty}^{\infty} h(\boldsymbol{\beta})h(\boldsymbol{\Lambda})R_{in}(\Delta\mathbf{r}+\beta-\Lambda)d\beta d\boldsymbol{\Lambda} =$$

$$= h(\Delta\mathbf{r}) \otimes h^*(-\Delta\mathbf{r}) \otimes R_{in}(\Delta\mathbf{r}) \tag{4.38}$$

The process is equivalent to the passage of the autocorrelation function $R_{in}(\Delta\mathbf{r})$ through two LSI systems cascaded in series. It is helpful to understand the effect of filtering the autocorrelation function in the spectral domain $\mathbf{k}$, where the autocorrelation becomes the input power spectral density and the relation between output and input power spectral densities is

$$S_{out}(\mathbf{k}) = | H(\mathbf{k}) |^2 \, S_{in}(\mathbf{k}) \tag{4.39}$$

Next we describe the filtering process of the 3-point autocorrelation function $E[\psi^*(\mathbf{r})\psi(\mathbf{r}+\Delta\mathbf{r}')\psi(\mathbf{r}+\Delta\mathbf{r}'')]$ by a generic LSI filter [35,41]. The relation between input and output triple autocorrelations is

$$R_{out}(\Delta\mathbf{r}', \Delta\mathbf{r}'') == h(\Delta\mathbf{r}) \otimes h(\Delta\mathbf{r}) \otimes h^*(-\Delta\mathbf{r}) \otimes R_{in}(\Delta\mathbf{r}', \Delta\mathbf{r}'') \tag{4.40}$$

which in the spectral domain is equivalent to the following input-output bispectra equation:

$$B_{out}(\mathbf{k}_1,\mathbf{k}_2) = H(\mathbf{k}_1)H(\mathbf{k}_2)H^*(\mathbf{k}_1+\mathbf{k}_2)B_{in}(\mathbf{k}_1,\mathbf{k}_2) \tag{4.41}$$

where

$$|B_{out}(\mathbf{k}_1,\mathbf{k}_2)| = |H(\mathbf{k}_1)\|H(\mathbf{k}_2)\|H^*(\mathbf{k}_1+\mathbf{k}_2)\|B_{in}(\mathbf{k}_1,\mathbf{k}_2)| \tag{4.42}$$

$$\angle B_{out}(\mathbf{k}_1,\mathbf{k}_2) = \angle H(\mathbf{k}_1)\angle H(\mathbf{k}_2)\angle H^*(\mathbf{k}_1+\mathbf{k}_2)\angle B_{in}(\mathbf{k}_1,\mathbf{k}_2) \tag{4.43}$$

A LSI system low-pass filters an input wavefield via its transfer function $H(\mathbf{k})$ thereby increasing the wavefield spatial autocorrelation $R(\Delta\mathbf{r})$. As long as the bandwidth of wavefield $\Delta\mathbf{k}_{in} \le \Delta\mathbf{k}_{system}$ the output spectral density $S_{out}(\mathbf{k})$ will be a scaled version of the input spectral density $S_{in}(\mathbf{k})$ as long as $|H(\mathbf{k})| = constant$ over $\Delta\mathbf{k}_{in}$ (ideal pass-band filter).

As long as $B_{in}(\mathbf{k}_1,\mathbf{k}_2) \neq 0$ for triads of wave-vectors $\mathbf{k}_1,\mathbf{k_2},\mathbf{k_3} = \mathbf{k_1}+\mathbf{k_2} \le \Delta\mathbf{k}_{system}$ the output bispectrum function $B_{out}(\mathbf{k}_1,\mathbf{k}_2)$ will be a scaled version of the input bispectrum $B_{in}(\mathbf{k}_1,\mathbf{k}_2)$ no matter $|H(\mathbf{k_1})|$, $|H(\mathbf{k_2})|$, $|H(\mathbf{k_1}+\mathbf{k_2})|$.

4.6.2 FREE SPACE PROPAGATION AS A LINEAR FILTER

All the physically realizable electromagnetic wavefields must be solutions to the general wave equation (WE). This dissertation discusses scalar, monochromatic wavefields with high directionality, i.e. low spatial divergence. These particular fields are called paraxial wavefields (or beams) and have the general form

$$\psi(\mathbf{r}) = A(\mathbf{r})exp(jk_0z) \tag{4.44}$$

where $k_0 = |\mathbf{k_0}| = \frac{2\pi}{\lambda_0}$, λ_0 the wavelength and $A(\mathbf{r})$ is the so called slowly varying envelope. A paraxial wavefield is analogous to a plane wave (perfect directionality) modulated by the complex amplitude $A(\mathbf{r})$ to give it a finite cross-section and finite energy[25]. The mathematically acceptable amplitudes $A(\mathbf{r})$ must be solutions of the parabolic paraxial wave equation (PWE)

$$\nabla_T^2 A(\mathbf{r}) + jk_0 \frac{\partial A(\mathbf{r})}{\partial z} = 0 \tag{4.45}$$

Instead of solving the paraxial wave equation, it is possible to study the phenomenon of paraxial wave propagation in free space using the theory of LSI systems and formulate the process of free space propagation as a filtering operation [51]. In the LSI framework an input wavefield $\psi(\mathbf{r})$ (and all its statistical measures) is filtered by the ``free space'' LSI system by means of its free-space impulse response

$$h(\mathbf{r}) \approx (\frac{j}{\lambda_0 z}) exp(jk_0 z) exp[jk_0 \frac{\mathbf{r^2}}{2z}] \tag{4.46}$$

which is the paraxial approximation to a spherical wave. The output wavefield $\psi_{out}(\mathbf{r})$ of the free-space system is obtained via the convolution integral

$$\psi_{out}(\mathbf{r}) = \psi_{in}(\mathbf{r}) \otimes h(\mathbf{r}) \approx \psi_{in}(\mathbf{r}) \otimes (\frac{j}{\lambda_0 z}) exp(jk_0 z) exp[jk_0 \frac{\mathbf{r^2}}{2z}] \tag{4.47}$$

The Fourier transform of $h(\mathbf{r})$ is the free-space transfer function $H(\mathbf{k_T})$

$$H(\mathbf{k_T}) = exp[jk_0 z] exp[-j(\frac{\mathbf{k_T^2}}{2k_0})z] \tag{4.48}$$

which is a function of the transverse wavevector $\mathbf{k_T} = (k_x \mathbf{x} + k_y \mathbf{y})$ and $k_0 = |\mathbf{k_0}|$ ($\mathbf{k}_0 = k_z \mathbf{z} + \mathbf{k_T} = k_z \mathbf{z} + (k_x \mathbf{x} + k_y \mathbf{y})$). The transfer function $H(\mathbf{k_T})$, being a function of $\mathbf{k_T}$,

is a reminder that the input-output relation of any LSI system can be specified in terms of complex sinusoids of frequencies $\mathbf{k_T}$ in the frequency domain, rather than using the convolutional approach with $h(\mathbf{r})$. The 2-dimensional input wavefield $\psi_{in}(\mathbf{k_T})$ at distance $z = 0$ can be written as a superposition (spectrum) of plane waves of the form

$$A(\mathbf{k_T}, z = 0) = E(\mathbf{k}_T) = Aexp[j(\mathbf{k_T} \cdot \mathbf{r})] \tag{4.49}$$

travelling in different $\mathbf{k_T}$ directions with complex amplitudes A. Plane waves are eigenfunctions of the ``free-space propagation'' system: propagation through a distance z is equivalent to multiplication of each plane wave in the input field $\psi(\mathbf{r})$ by system transfer function $H(\mathbf{k_T})$ which represent the eigenvalues as a function of $\mathbf{k_T}$:

$$A(\mathbf{k_T}, z) = H(\mathbf{k_T})A(\mathbf{k_T}, z = 0) \tag{4.50}$$

For paraxial plane waves with $|\mathbf{k_T}| \ll k_0$

$$A(\mathbf{k_T}, z) = Aexp[j\mathbf{k_T} \cdot \mathbf{r}]exp[jk_0 z]exp[-j(\frac{\mathbf{k_T^2}}{2k_0})z] \tag{4.51}$$

The function $A(\mathbf{k_T}, z)$ shows how each 2-dimensional plane wave in the plane $z = 0$ has gained in the plane $z = z$ a new phase term that is nonlinear with spatial frequency vector $\mathbf{k}$:

$$\Phi(\mathbf{k}) \propto \mathbf{k_T^2} \tag{4.52}$$

This $\mathbf{k}$ squared dependent phase term is the cause of new phase relations between plane waves at the plane z. This dephasing causes the field to spatially spread [44,51]. Note that the free-space transfer function $H(\mathbf{k_T})$ has modulus unity up to a certain cut-off spatial frequency $\mathbf{k}$: only plane waves with spatial frequency $\mathbf{k_T} | < \frac{2\pi}{\lambda}$ will be passed

unattenuated. Waves with $|\mathbf{k_T}| \geq \frac{2\pi}{\lambda}$ are called evanescent plane waves and decay quickly (the faster the higher $|\mathbf{k}|$) in the z direction so they don't participate in paraxial propagation: $H(\mathbf{k_T}) = 0$ for $\mathbf{k_T}| \geq \frac{2\pi}{\lambda}$. The phenomenon of paraxial free-space propagation is analogous to a spatially dispersive low-pass filter passing having a finite spatial bandwidth $\Delta\mathbf{k_T} < \frac{2\pi}{\lambda}$. The creation of partially spatially coherent wavefields with nonzero bispectral characteristics is one the objective of this work. Free-space propagation, being equivalent to a LSI system, will propagate the bispectrum of the input field without alteration. Any information encoded in the bispectrum (as long as the bispectrum support is within $\Delta\mathbf{k_T} < \frac{2\pi}{\lambda}$) is passed unaltered and can be recovered. Besides the remarkable property of being insensitive to additive Gaussian noise (regardless of its mean, variance and power spectrum), the bispectrum offers an extra useful degree of freedom for encoding information.

4.7 GENERATION OF A PARTIALLY COHERENT WAVEFIELD WITH BISPECTRAL PROPERTIES

The starting point for the generation of a partially coherent wavefield is an input wavefield with Gaussian amplitude and delta-correlated wavefront $\zeta(x, y)$ (delta spatial two-point autocorrelation function) with standard deviation σ_r.

The wavefront $\zeta(x, y)$ is then filtered with a Gaussian function $f(x, y)$ to create a partially correlated wavefront [45,46,54]. The wavefield has then an autocorrelation function equal to

$$R(\eta,\xi) = exp\{-\frac{\sigma_r^2}{4\pi\sigma_f^2}[1-exp(-\frac{\Delta\eta^2+\Delta\xi^2}{4\sigma_f^2})]\} \tag{4.53}$$

If of the standard deviations σ_f and σ_r are such that $\frac{\sigma_r^2}{4\pi\sigma_f^2} \gg 1$ the autocorrelation function assumes a Gaussian form:

$$R(\Delta\eta,\Delta\xi) \approx exp[-\frac{(\Delta\eta^2+\Delta\xi^2)}{2\ell_{coh}}] \tag{4.54}$$

where $\ell_{coh}^2 = \frac{8\pi\sigma_f^4}{\sigma_r^2}$ is the correlation length. Following this method we created a field that represents a single realization of a partially spatially coherent wavefield with circular, Gaussian shape correlation function and finite coherence area.

The angular spectrum of this partially coherent input wavefield was designed so that certain spectral components with spatial wave vectors of magnitude $|\mathbf{k}_n| = k_n$ residing on three rings of radii $k_1 = |\mathbf{k_1}|, k_2 = |\mathbf{k}_2|, k_3 = |\mathbf{k}_3|$ in the k-plane were statistically related via quadratic phase coupling.

The statistical dependence occurs isotropically in the phase spectrum along each radial direction: for any radial direction at angle α the spatial wave vectors $\mathbf{k}_1$ and $\mathbf{k}_2$ on the first ring and second ring respectively have random phases whose sum is always equal to the random phase of the spatial wave vector $\mathbf{k}_3$ on the third ring along the same line: $\theta_3 = \theta_1 + \theta_2$ and the sum of the x-components of $\mathbf{k}_1$ and $\mathbf{k}_2$ sum up to the x-component of $\mathbf{k}_3$. The same is true for the y-components.

In the analytical case the three rings are supposed to have infinitely small thickness, i.e. two-dimensional delta rings of the form $\frac{1}{2\pi k}\delta(k-k_n)$.

In the numerical simulation the three wave vector rings were given a finite thickness of two, two and three pixels respectively. The finite thickness was required in order to trace continuous rings without missing pixels. For example, in the phase spectrum, for the radial line making an angle α with the horizontal axis, the two pixels composing the first ring are labeled K00 and K01, the pixels composing the second ring K10, K11 while those forming the third ring K20, K21, K22. Quadratic phase coupling was prescribed by setting the random phase value at pixel K20 equal to the phase of pixel K00 plus the phase at pixel K10. The following Figure shows how the phase values at different pixels are related:

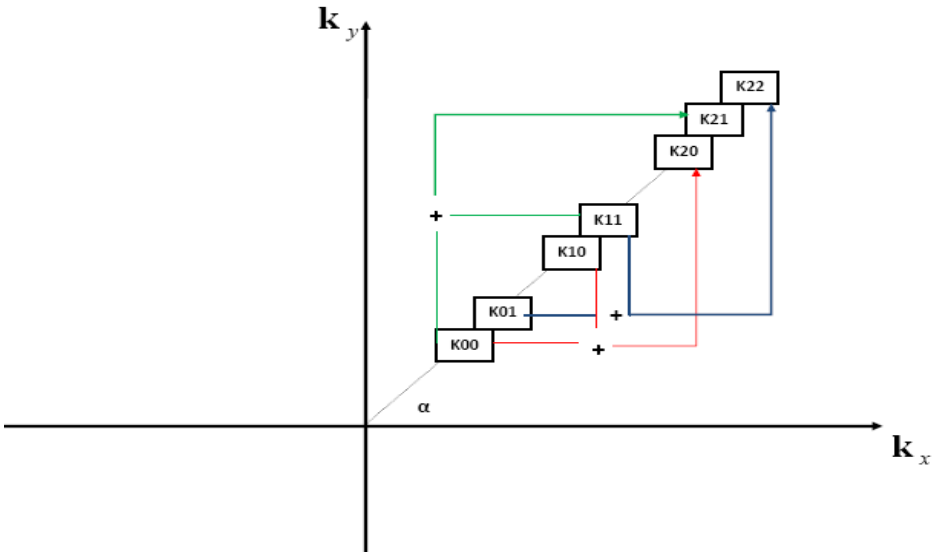

Fig. 4.4 Phase spectrum of the angular spectrum: pixels lying on the three rings along an arbitrary radial line

In the continuous case there are infinite possible radial directions in the angular spectrum on which to examine correlations among spectral components. In the discrete case the phase spectrum is subdivided into a finite number of angular sectors (1024) of width $\Delta\theta$.

For every sector $\Delta\theta$ there are three sets of pixels: (K00, K10, K20), (K01, K11, K22) and (K00, K11, K21). The coordinates of each pixel represent the wave vectors components. The wave vectors in each set have phases related via quadratic phase coupling and show a nonzero bicoherence (normalized bispectrum).

This means that three bicoherence values were calculated for each angular sector $\Delta\theta$, one for the wave vectors in set (K00, K10, K20), and two for values for the other two sets.

Quadratic phase coupling and consequent nonzero bispectral characteristics were inscribed on a partially coherent input wavefield with Gaussian autocorrelation function and far field Gaussian irradiance (Gauss-Schell model).

The chart below explains the steps followed in the process of creation of phase correlation/bispectrum in the angular spectrum of the input wavefield:

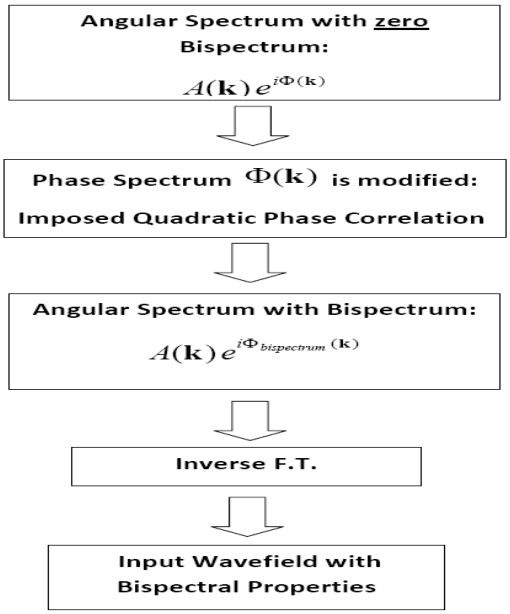

Fig. 4.5 Process of creation of nonzero bispectrum in the input wavefield

4.8 PARAXIAL PROPAGATION METHOD FOR PARTIALLY COHERENT WAVEFIELDS

The approach used to numerically simulate the paraxial propagation of partially coherent wavefields is based on Fourier methods [52,53,54].

Multiple (600) different wavefield realizations were generated following the method described above. Each field realization was then propagated into the far-field at a distance $z >> \frac{2D^2}{\lambda}$, where D is the nominal diameter of the wavefield aperture (width of the Gaussian amplitude) and λ the radiation wavelength.

4.9 RETRIEVAL OF BISPECTRUM AFTER PROPAGATION

After propagation in the far field, the bispectral properties of the partially coherent wavefield were extracted and compared to the bispectral properties before propagation.

The angular spectrum of each partially coherent wavefield realization was first calculated. The triple product was computed among those spectral components that were set in the input wavefield to be in quadratic phase coupling.

Those spectral components are the ones lying on the three rings and in phase coupling with those components along the same radial direction on the other rings.

The procedure is repeated for the 600 propagated wavefield realizations and the ensemble average of all the triple products was carried out to determine the bicoherence properties of the propagated field.

Numerical simulations support the analytical prediction that the bispectrum is invariant upon free space propagation: quadratic phase coupling (nonzero bispectrum) was a priori imposed on the input partially coherent wavefield before propagation.

We knew beforehand which spectral components were in fixed phase correlation (since we intentionally designed those spectral components to be so in the input field). We simply returned to those spectral components in the angular spectrum of the propagated wavefield and checked if the phase correlation was preserved. All the quadratic phase correlations predetermined in the input field were found to be intact and recovered.

4.10 SIMULATIONS AND NUMERICAL RESULTS

Input Wavefield:

The parameters of the partially spatial coherent input wavefield were:

- Wavelength: 632.9 nm;
- Diameter: 4 cm;
- Spatial correlation length: 5 mm.

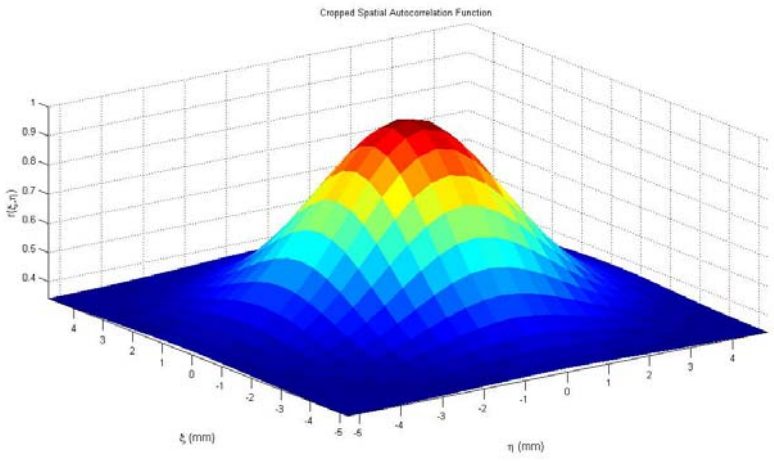

Fig. 4.6 Cropped autocorrelation function

The following figures show the angular phase spectrum of the input partially coherent wavefield. Figure 4.6 shows a phase spectrum with no bispectral dependencies among wave vectors:

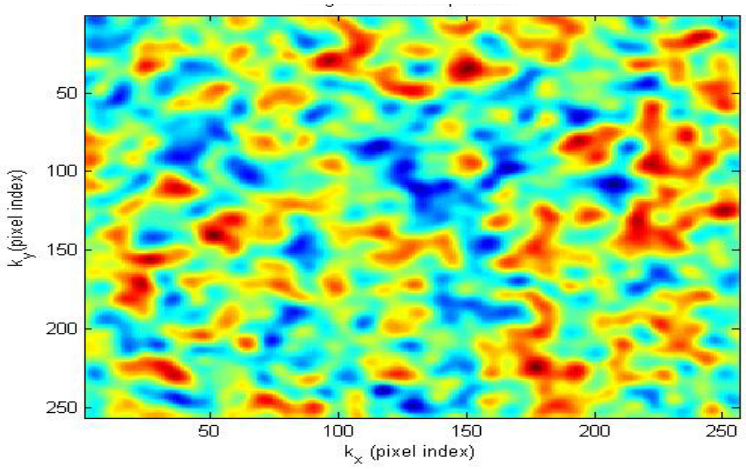

Fig. 4.7 Angular phase spectrum of the input wavefield

Figure 4.7 shows the phase spectrum after quadratic phase correlations have been established among spectral components lying on three rings in k-space. The third ring is clearly evident:

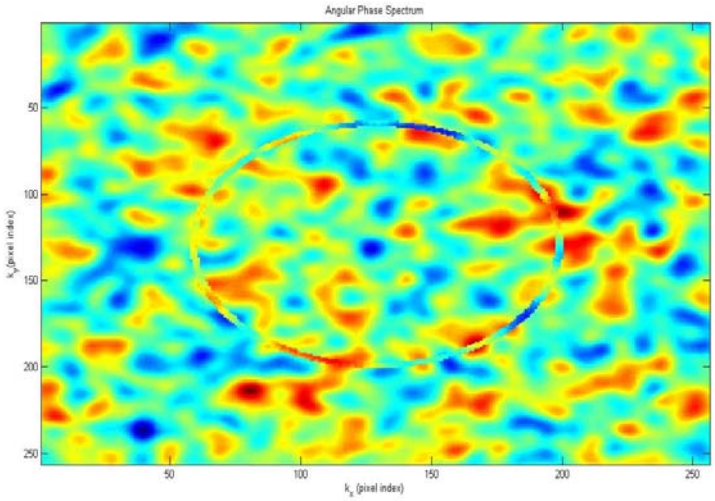

Fig. 4.8 Angular phase spectrum with phase correlations

The three rings in the phase spectrum over which phase correlations exist are isolated in the next figure for clarification purposes:

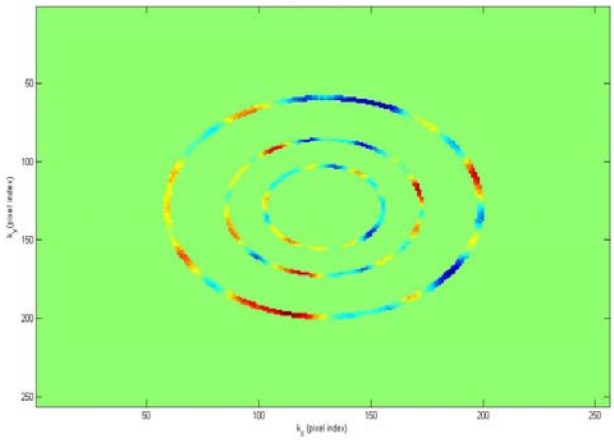

Fig 4.9 Three correlated rings in the phase spectrum

Propagated Wavefield:

The input partially coherent wavefield was propagated in free space over a distance of 1000m. The simulated propagation of the field with bispectral properties shows a quasi-Gaussian irradiance function with a transverse spread (≈ 5 cm) very close to the analytically expected one. The simulation of the free space propagation process was accomplished using Fourier transform methods well described in [46,53,54].

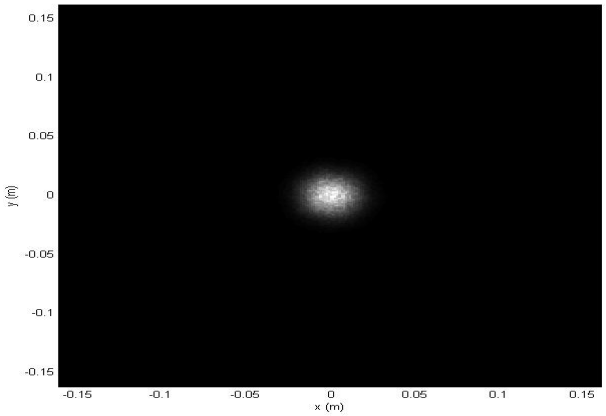

Fig 4.10 Irradiance for the partially coherent field after a 1km propagation distance

In order to quantify the bispectral properties of such wavefield the ensemble average of the triple product over 600 field realization was calculated for 1024 angular

sectors along the radial direction. The next figure shows the bicoherence value for the three spectral components with wave vector magnitudes K00, K10, K20. The horizontal axis represents the angular position $\Delta\theta$ for each radial direction:

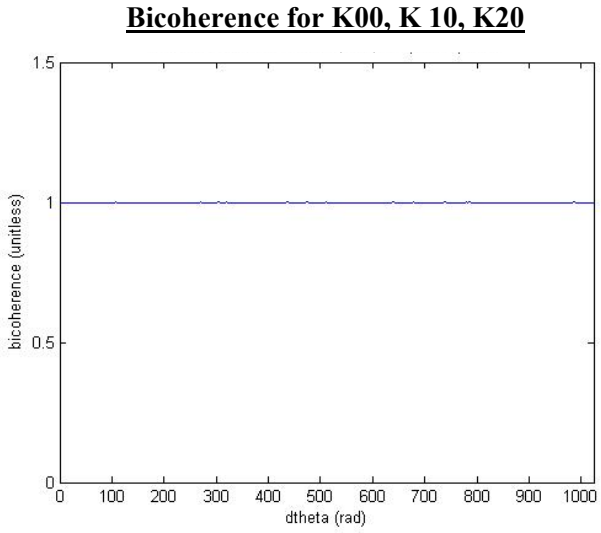

Fig. 4.11 Bicoherence values for 3 spectral components with wave vectors K00, K10, K20 for angles that are multiples of $d\theta$.

The unit bicoherence is also calculated for the other two sets of spectral components lying along a radial direction. Figure shows how for each angle $d\theta$ the set of three spectral components are fully correlated (maximum bicoherence):

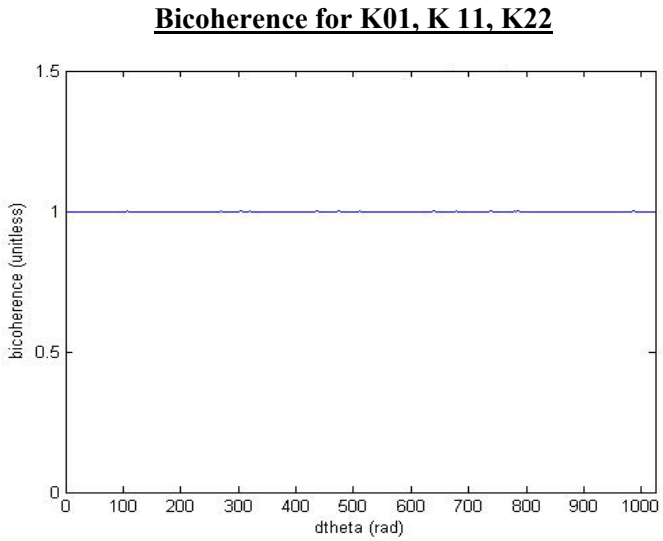

Fig. 4.12 Bicoherence values for 3 spectral components with wave vectors K01, K11, K22 for angles that are multiples of $d\theta$

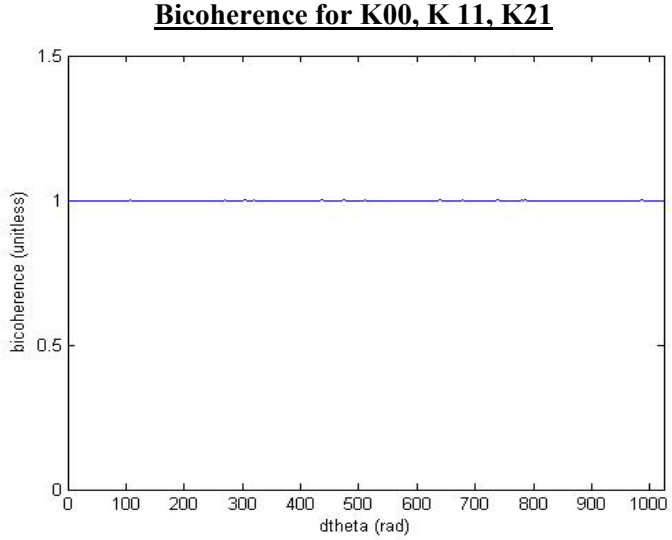

Fig. 4.13 Bicoherence Values for 3 spectral components with wave vectors K00, K11, K21 for angles that are multiples of $d\theta$

The free space propagation process does not erase the quadratic phase correlations still visible in the propagated angular phase spectrum:

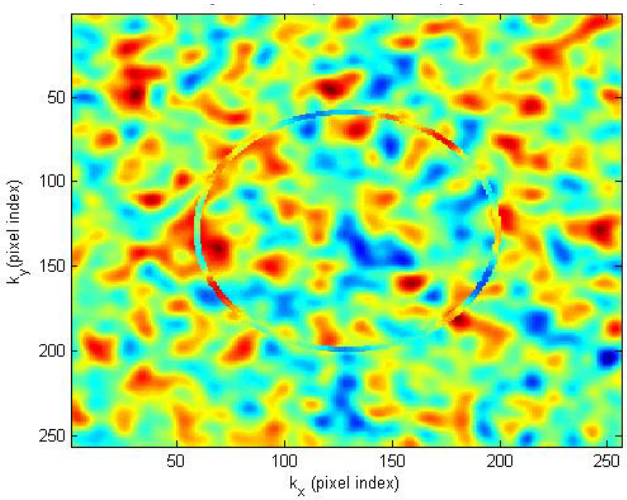

Fig. 4.14 Angular phase spectrum after propagation

4.11 PROPOSED EXPERIMENTAL METHOD FOR GENERATING BISPECTRAL WAVEFIELDS

Spatial Filtering is a Fourier optics technique used to modulate the amplitude and phase of a wavefield for various applications (pattern recognition, image processing, holography, microscopy, etc…)

A spatial filtering set up can be used for creating a partially coherent wavefield with a bispectral signature from a fully coherent input field with no bispectral properties [30]. A transmission phase/amplitude spatial light modulator (SLM) is placed at the focal plane of a 4-F system formed by two positive lenses with focal length F.

The 4-F system allows manipulation of both the amplitude and phase of the input angular spectrum. Hence the phase spectrum can be modified: the SLM would generate an angular spectrum modulation mask with prescribed quasi-random amplitude and phase. The phase modulation will not be completely random: it will contain quadratic

phase coupling relations for those spectral components lying on three properly spaced concentric rings. This approach will result in an output wavefield with bispectral features.

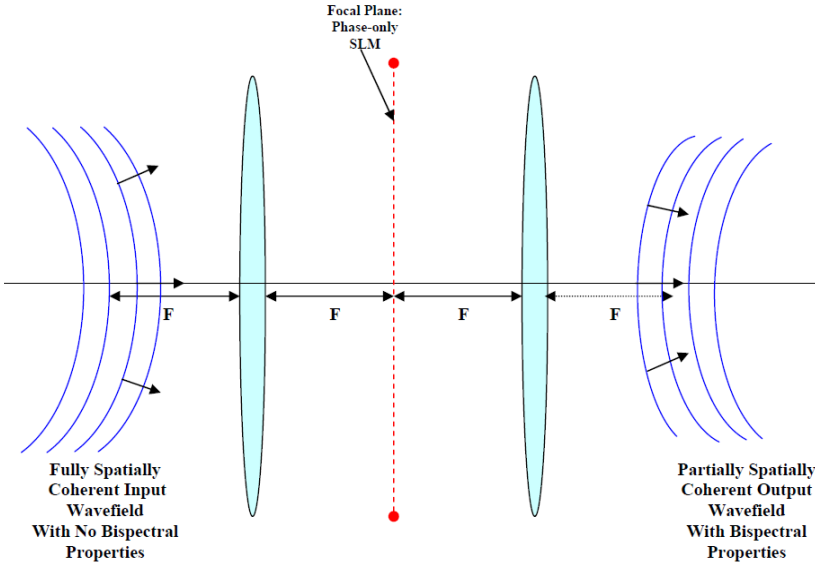

Fig. 4.15 Spatial filtering set-up for bispectral wavefield generation

CHAPTER 5: CONCLUSIONS

There are many areas of research that are interested in developing electromagnetic wavefields with customizable properties tailored to specific applications. Phase, amplitude and polarization are the three degrees of freedom that can be controlled to achieve wavefields with desired characteristics.

This dissertation focused on wavefields with nontrivial phase structure. Optical vortex beams are an example of fully spatially coherent paraxial wavefields with helicoidal wavefronts. This type of beams has received wide attention due to their resilience during propagation in turbid media. Since vortex beams are becoming important for many applications, the development of new and improved vortex beam generation methods is becoming important as well.

The first contribution of this dissertation consists in the novel and successful use of a 37 actuator segmented deformable mirror for the generation of optical vortex beams with topological charge from 1 to 10. The segmented deformable mirror offers a valid alternative to other methods for creating vortices with arbitrary integer of fractional charge. The deformable mirror technology is advancing at a rapid pace. New DM systems with 313 segments are now available. Update rates of 30 kHz are possible with FPGA interface hardware, and the use of dielectric coatings will extend the use of

segmented DMs to high power and pulsed applications where other methods are not suitable.

The deformable mirror has the advantage of being dynamic and polarization independent. The use of rectangular segments instead of hexagonal ones along the jump discontinuity of the mirror is a feasible upgrade that will significantly improve the quality of the generated optical vortices.

In conjunction with the work on the deformable mirror an optical vortex mode purity comparison between the mirror and multi-step diffractive phase plates with 16 and 32 discrete steps was carried out both analytically and in simulation. The comparison was carried out in order to validate the use of the DM for vortex beam applications. The SPP was used as a performance benchmark.

Computer simulations show the intensity and phase of the vortices generated with the two methods (DM and SPP). The deformable mirror, by being reconfigurable, can generate optical vortices with higher mode purity, while the static phase plate mode efficiency declines due to the fixed number of phase steps. The mode purity comparison evaluates the performance of the deformable mirror for applications requiring high charge optical vortices. These results support the adoption of the DM as a versatile device in vortex beam applications.

The third contribution of this research work presents and validates the possibility of creating phase structured wavefields that are not fully spatially coherent like the optical vortex beams generated with the DM but partially spatially coherent beams with nonzero bispectral characteristics. These wavefields show an inherent statistical phase structure due to a nonzero bispectrum.

The bispectrum has always been used as a statistical measure to characterize received data or to identify the nonlinear properties of the system that processed the data.

The approach I used explicitly engraved a bispectral signature in the input wavefield before propagation. Numerical simulations showed that the engraved bispectral properties are invariant upon propagation in free space. The performed simulations assumed that the bispectral content was written and retrieved directly in the electric wavefield. This is possible only in applications where it is feasible to deal with the electric field directly (microwave or radio regime).

In the optical regime the electric field oscillates too fast, but the same bispectral information encoding approach can still be used by recording multiple realizations of the instantaneous irradiance.

Partially spatially coherent wavefields have been shown to be very robust in several propagation scenarios (propagation through atmospheric turbulence).

The design of partially spatial coherent wavefields with nonzero bispectrum can lead to new wavefields with better propagation characteristics. A simple 4-F spatial filtering system can be used to experimentally create fields with bispectral signature.

Under this new light the bispectrum is no longer just a statistical analysis to characterize information and channel properties, but becomes a new degree of freedom for encoding information in a wavefield.

REFERENCES

1. N. B. Baranova and B. Ya. Zel'dovich, "Dislocations of the wave-front surface and zeros of the amplitude," *Zh. Eksp. Teor. Fiz*., vol.80, pp. 1789–1797, 1981.

2. V. Basistiy, M. S. Soskin, and M. V. Vasnetsov, "Optical wavefront dislocations and their properties," *Opt. Commun.,* vol.119, pp.604–612, 1995.

3. V. Y. Bazhenov, M. V. Vasnetsov, and M. S. Soskin, "Laser beams with screw dislocations in their wavefronts" *JETP Lett., vol.* 52, pp. 429–431, 1990.

4. C. Paterson, "Atmospheric turbulence and orbital angular momentum of single photons for optical communication," *Phys. Rev. Lett.* , vol. 94, id. 153901, 2005.

5. G. Gbur and R. K. Tyson, "Vortex beam propagation through atmospheric turbulence and topological charge conservation," *J. Opt. Soc. Am. A,* vol. 25, pp. 225-230, 2008.

6. M. V. Vasnetsov, I. G. Marienko, and M. S. Soskin, "Self-reconstruction of an optical vortex," *JETP Lett.,* vol.71, pp.130–133, 2000.

7. Marco Scipioni, "Propagation of optical vortices through fog", Thesis (M.S.)--University of North Carolina at Charlotte, 2004.

8. N. R. Heckenberg, R. McDuff, C. P. Smith, and A. G. White, "Generation of optical phase singularities by computer-generated holograms," *Opt. Lett.* , vol. 17, pp. 221, 1992.

9. M. D. Levenson, T. Ebihura, G. Dai, Y. Morikawa, N. Hyashi, and S. M. Tan, "Optical vortex mask via levels," *J. Microlithogr. Microfabr. Microsyst.,* vol. 3, pp. 293–304, 2004.

10. C. S. Guo, D. M. Xue, Y. J. Han, and J. Ding, "Optimal phase steps of multi-level spiral phase plates", *Opt. Commun.,* vol. 268, 235–239, 2006.

11. S. S. R. Oemrawsingh, J. A. W. van Houwelingen, E. R. Eliel, J. P. Woerdman, E. J. K. Verstegen, J. G. Kloosterboer, and G. W. 't Hooft, " Production and Characterization of Spiral Phase Plates for Optical Wavelengths," *Appl. Opt.* vol. 43, pp. 688-694, 2004.

12. M. B. Fleming and M. C. Hutley, “Blazed diffractive optics,” *Appl. Opt.,* vol.36, pp.4635–4643, 1997.
13. V. V. Kotlyar, A. A. Almazov, S. N. Khonina, V. A. Soifer, H. Elfstrom, and J. Turunen, "Generation of phase singularity through diffracting a plane or Gaussian beam by a spiral phase plane," *J. Opt. Soc. Am. A.,* vol. 22, pp.849-861, 2005.

14. D. C.O'Shea, A. D. Kathman, and T. J. Suleski, *Diffractive Optics: Design, Fabrication, and Test* (SPIE-International Society for Optical Engineering, 2003).

15. Z. Jaroszewicz, A. Kołodziejczyk, A. Kowalik, and R. Restrepo, “Determination of phase step errors of kinoform gratings from their diffraction efficiencies,” *Opt. Eng.*, vol. 40, pp.692–697, 2001.

16. R. K. Tyson, M. Scipioni, and J. Viegas, “Generation of an optical vortex with a segmented deformable mirror,” *Appl. Opt.,* vol. 47, pp. 6300-6306, 2008.

17. M. A. Helmbrecht, T. Juneau, M. Hart, and N. Doble, “Segmented MEMS deformable-mirror technology for space applications,” *Proc. SPIE*, vol.6113, pp.622–305, 2006.

18. J. Leach, E. Yao, and M. J Padgett, “Observation of the vortex structure of a non-integer vortex beam,” *New J. Phys.,* vol.6, pp.71-78, 2004.

19. S.S.R. Oemrawsingh, E.R. Eliel, J.P. Woerdman, J.K. Verstegen, J.G. Kloosterboer and G.W. 't Hooft, "Half integral spiral phase plates for optical wavelengths", *J.Opt.A: Pure Appl. Opt*. vol.6, 2004.

20. W. M. Lee, X.-C. Yuan, and K. Dholakia, “Experimental observation of optical vortex evolution in a Gaussian beam with an embedded fractional phase step,” *Opt. Commun.* vol. 239, 129, 2004.

21. M V Berry, “Optical vortices evolving from helicoidal integer and fractional phase steps,” *J. Opt. A: Pure Appl. Opt.,* vol.6, pp. 259-268, 2004.

22. G. Molina-Terriza, J. Recolons, and L. Torner, “The curious arithmetic of OVs,” *Opt. Lett.* , vol. 25, pp. 1135–1137, 2000.

23. J. Visser and G. Nienhuis, "Orbital angular momentum of general astigmatic modes,*" Phys. Rev. A*, vol. 70, id. 013809, 2004.

24. J. A. Arnaud and H. Kogelnik, “Gaussian Light Beams with General Astigmatism*,” Appl. Opt.*, Vol. 8, Issue 8, pp. 1687-1693, 1969.
25. A. W. Lohmann, D. Mendlovic and Z. Zalevsky,”Fourier Optics of the Triple Correlation, “Opt. *Commun.*, vol. 152, pp. 243-246, 1998.

26. A. W. Lohmann, D. Mendlovic, and G. Shabtay, "Coherence waves," *J. Opt. Soc. Am. A*, vol. 16, pp. 359-363, 1999.

27. A. W. Lohmann, B. Wirnitzer , “Triple correlations,” *Proc of the IEEE,* vol.72, pp. 889, 1994.

28. A.W. Lohmann, G. Weigelt, and B.Wirnitzer, "Speckle masking in astronomy: triple correlation theory and applications," *Appl. Opt.*, vol. 22, pp. 4028-4037, 1983.

29. H. Bartelt, A. W. Lohmann, and B. Wirnitzer, "Phase and amplitude recovery from bispectra," *Appl. Opt.* vol.23, pp. 3121-3129, 1984.

30. J. Goodman, *Introduction to Fourier Optics*, 3rd ed., Roberts & Company, 2004.

31. D. R. Brillinger, "An introduction to polyspectra," *Annals of Mathematical Statistics*, Vol. 36, pp. 1351-1374, 1965.

32. D. R. Brillinger, M. Rosenblatt, "Computation and interpretation of k-th order spectra", *Spectral Analysis of Time Series*, pp.189-232, 1967.

33. H. Akaike, “Note on Higher-Order Spectra”, *Ann. Inst. Statist. Math.*, vol.18, pp.123-126, 1966.

34. M. J. Hinich, "Testing for Gaussianity and Linearity of a Stationary Time Series”, *J. Time Series Analysis*, vol. 3, pp.169-176, 1982.

35. C. L. Nikias, A. P. Petropulu, *Higher-Order Spectral Analysis: A Nonlinear Signal Processing Framework*, Prentice Hall, 1993.

36. S.L. Marple, *Digital Spectral Analysis*, Prentice Hall, 1987.

37. J. M. Mendel, *“*Tutorial on Higher-Order Statistics *(*Spectra) in Signal Processing and System Theory*:* Theoretical Results and Some Applications*", IEEE Proc.*, vol. 79, pp. 278-305, 1991.

38. S.M. Kay, *Modern Spectral Estimation*, Prentice Hall, 1988.

39. M. B. Priestley, *Spectral Analysis or Time Series*, Academic, 1981.

40. A.V Oppenheim, J.S Lim "The Importance of Phase in Signals", *Proceedings of the IEEE*, Vol. 69, 529-541, 1981.

41. C. W. Therrien*, Discrete Random Signals and Statistical Signal Processing,* Prentice Hall, 1992.

42. J.W.A. Fackrell, A.G. Stogioglou, S. McLaughlin, "Robust Frequency-Domain Bispectrum Estimation,", *8th IEEE Signal Processing Workshop on Statistical Signal and Array Processing*, pp.206, 1996.

43. W.B. Collis, P. White, J. Hammond, "Higher Order Spectra*:* the bispectrum and trispectrum", *Mechanical Systems and Signal*. *Processing*, vol. 12, pp.*375*-395, *1998.*

44. A. Ishimaru, *Wave propagation and scattering in random media*, Academic press, 1978.

45. M.C.Roggemann and B.M.Welsh, *Imaging Through Turbulence*, CRC Press, 1996.

46. L.C.Andrews and R.L.Phillips, *Laser Beam Propagation through Random Media*, SPIE Press, 2005.

47. T. Matsubara, "Phase Correlations in Non-Gaussian Fields," *The Astrophysical Journal*, vol. 591, L79–L82, 2003.

48. T. Matsubara, "Statistics of Fourier Modes in Non-Gaussian Fields", *The Astrophysical Journal Supplement Series*, vol.170, pp.1-32, 2007.

49. P. S. Naidu*, Modern Spectrum Analysis of Time Series*, CRC Press, 1996.

50. W. W.S. Wei, *Time Series Analysis Univariate and Multivariate Methods,* Addison Wesley, 1990.

51. B.E.A Saleh and M.C. Teich, *Fundamentals of Photonics*, Wiley, 1991.

52. S.V. Narasimhan, S. Veena*, Signal Processing Principles and Implementation*, Narosa Publishing House, 2005.

53. J. D. Schmidt, *Numerical Simulations of Optical Wave Propagation*, SPIE Press, 2010.

54. X. Xiao, D. Voelz, “Wave optics simulation approach for partial spatially coherent beams”, O*pt. Express*, vol. 14, pp.6986-6992, 2006.